Excess Conductivity Analysis and Magneto-resistance Measurements of $Cu_{0.5}Tl_{0.5}Ba_2(Ca_2\text{-}yMg_y)(Cu_{2.5}Cd_{0.5})O_{10-\delta}$ (y=0, 0.25, 0.5) Samples.

Mehwish Parveen

Department of Physics

Quaid-i-Azam University

Islamabad, Pakistan

2023

Excess Conductivity Analysis and Magneto-resistance Measurements of $Cu_{0.5}Tl_{0.5}Ba_2(Ca_2\text{-}yMg_y)(Cu_{2.5}Cd_{0.5})O_{10-\delta}$ (y=0, 0.25, 0.5) Samples.

A dissertation submitted to the department of physics, Quaid-i-Azam University, Islamabad, in the partial fulfilment of the requirement for the degree of

Master of Philosophy

In

Physics

By

Mehwish Parveen

To the

Material Science Laboratory

Department of Physics

Quaid-I-Azam University

Islamabad, Pakistan

2023

In the name of Allah Almighty the most beneficent and merciful, and the most sovereign among all of us.

Certificate

This is to certify that **Ms. Mehwish Parveen D/O Fateh Muhammad** has carried out the experimental work in this dissertation under my supervision in **Materials Science Laboratory**, Department of Physics, Quaid-i-Azam University, Islamabad, and satisfying the dissertation requirement for the degree of Master of Philosophy in Physics.

Supervisor

Dr. Nawazish Ali Khan

Department of physics

Quaid-i-Azam University

Islamabad, Pakistan.

Submitted Through

Chairman

Dr. Kashif Sabeeh

Department of Physics Quaid-i-Azam University Islamabad,

Pakistan

Dedicated

To

Late Mother, Sister (Shaista Jabeen)

Abstract:

We have studied the excess conductivity analysis and magneto-resistance of $Cu_{0.5}Tl_{0.5}Ba_2(Ca_2$-$yMg_y)(Cu_{2.5}Cd_{0.5})O_{10-\delta}$ (y=0, 0.25, 0.5) samples. Main objective of such studies is the role of decreased inter-CuO_2 /CdO_2-plane distance in developing the phase coherence of carriers in various superconducting planes in such superconductors. Volume of the unit cell increases and their c-axes lengths suppress in such superconductors with increased Mg doping showing enhancement of inter-plane couplings. Since such superconducting planes have Cd atoms that is heavier than Cu atoms and therefore produce an-harmonic oscillations that induces the pair breaking effects in the final compound. Room temperature resistivity of doped samples increases whereas their T_c(R=0) suppresses in doped samples. The zero resistivity critical temperature is shifts towards lower temperatures with increased strength of applied magnetic fields showing thermally activated flux flow across the pinning centers. The energy of activation such thermally activated flow suppresses with increased Mg-doping and enhance strength of applied field. Excess conductivity analyses of resistivity data of Mg-doped samples have shown increase in the coherence length along the c-axis, Fermi-velocity of carriers and critical current density. Thermodynamic critical field B_c, lower critical field B_{c1} increases whereas the London penetration depth suppresses in Mg-doped samples showing increased population of the pinning centers.

Table of Contents

List of Figures

List of Tables

Chapter N0: 01

Introduction to Superconductivity

The origins of the superconductivity phenomenon, its brief historical history, and numerous theories that provide light on the phenomenon are all covered in this chapter. The chapter comes close with a number of superconducting applications.

1.1: Superconductivity

By gradually cooling certain metals and alloys to a certain temperature, their resistance decreases to zero. This wonder is known as superconductivity, and the substances that exhibit it are known as superconductors [1]. The temperature at which the shift from normal to superconductive state occurs is entitled as critical temperature and is denoted as Tc.

Superconductivity is a rescindable procedure, that is, on falling temperature of material below Tc, its state alters from normalconducting to superconducting state whereas on expanding the temperature above Tc, it undertakes the phase transition from superconducting to the normal state. This phase change also happens when the compound is put in a magnetic field [2].

1.2: Discovery and Evolution of superconductivity

H. Kamerlingh Onnes discovered superconductivity in 1911 while conducting the first low-temperature calculations to liquefy helium. He discovered that uncontaminated Hg's resistance reached zero at 4K when computing its resistivity. He discovered that the resistive state is in 1912 rehabilitated at high transport currents or in a magnetic field [3]

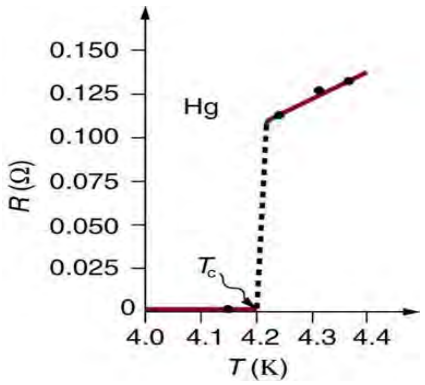

Fig 1.1: Temperature dependence of resistance in Hg

In Nb_3Ge, scientists had initially only reached Tc ~23 K, but they had hoped to get as close as possible to the critical temperature of 77 K. The search for high-temperature superconductors lasted until 1986, when G. Bednorz and A. Muller made the breakthrough discovery of a superconductor $La_{2-x}Ba_xCuO_4$(ceramic) Tc~30 K. As a result, a new family of superconductors with Tc higher in 1987, Y-Ba-Cu-O than was created. Later metallic superconductors with Tc~93K was developed. In thallium cuprates, which were found in 1988 Tc increased to 125K.

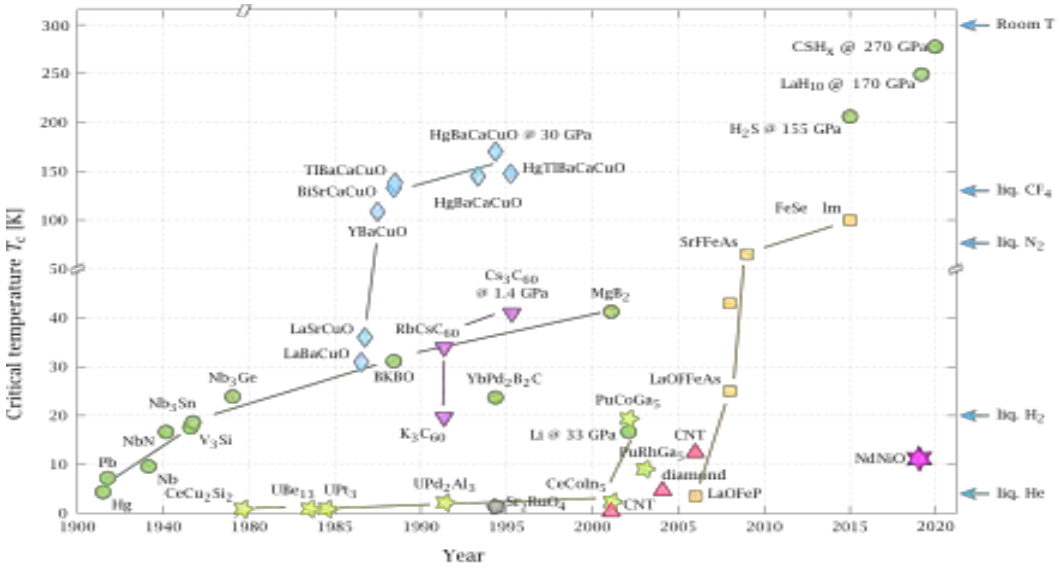

Fig 1.2: History of Superconductivity

1.3 Essential properties of superconductors

1.3.1 Zero Resistivity

At any temperature below the critical temperature, every superconductor exhibits zero resistance. The material conducts electricity perfect in this state. By creating a little dc current in a superconducting ring. Over the course of the experiment's 2.5 years, there was no noticeable current degradation. This indicates that the superconductor's resistivity is less than 10^{-23} Ωm. Compared to the resistivity of copper at normal temperature, this is 18times less than normal conductivity. This current's decay time can be computed to be greater than as 10^5 years [4].

Resistivity is characterized as

$$\rho = \frac{m_e}{n\tau e^2} \qquad (1.1)$$

where m_e is the electron's mass, n is the density of electrons, and τ is the electron's mean free time. As a result, the relationship between ρ and the average free time is inverse.

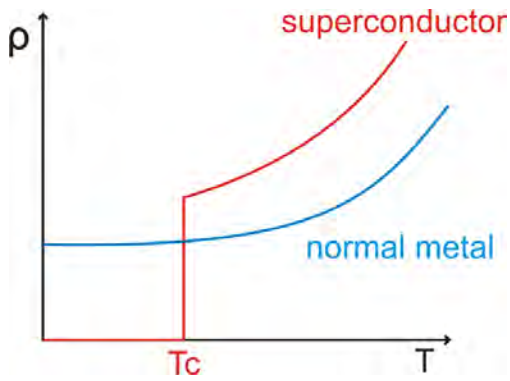

Fig 1.3: Temperature Vs Resistivity curves

1.3.2 Meissner Effect

Superconductors were thought to be the best conductors for a very long time. When a perfect conductor is cooled to its critical temperature and then exposed to an external magnetic field, it possesses diamagnetic behavior. Due to Lenz's law, which states that magnetic fields produce in opposite directions, the external magnetic field cannot penetrate the material when an induced current is present.

Let's look at it numerically.

According to Maxwell's Equation,

$$E = -\frac{1}{C}\frac{\partial B}{\partial t} \qquad (1.2)$$

As we are aware of

$$E = \rho_j$$

For perfect conductors ρ = 0

$$\frac{\partial B}{\partial t} = 0$$

B = constant (1.3)

As we had no magnetic field inside the conductor before applying the external magnetic field so according to Eq. 1.3, there will be no magnetic field afterwards also.

After introducing an external magnetic field, cooling the conductor will result in a finite amount of resistivity and field will enter the conductor. According to equation (1.3) the magnetic field will still be present inside the material after cooling. But a superconductor is an exception to this rule. As illustrated in figure, a superconductor has no magnetic field, regardless of whether an external field is provided before or after the material is cooled. The effect is known as Meissner effect.[5]

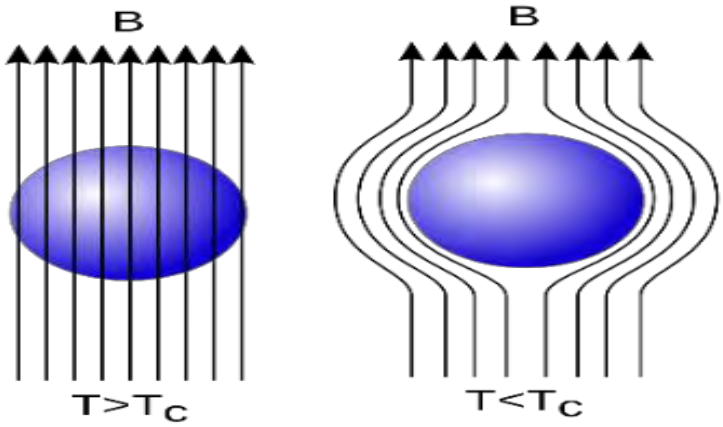

Fig 1.4: Meissner Effect

1.4 Parameters Relating Superconductivity

1.4.1 Critical Temperature T_c

At room temperature (290 K), the superconducting material is in a normal state, however current dissipation occurs because of electrical resistance (collision of electrons with atoms). A superconductor's electrical resistance quickly vanishes when it is cooled below a particular temperature, and the substance is termed to a superconductor. The temperature at which a superconductor's electrical resistance abruptly decreases to zero is known as the critical temperature, or T_c.

Material	Critical Temperature T_c (K)
Hg	4.2
C_6Ca	11.5
V_3Si	17.1
$TlSrLaCuO_5$	40
$YBa_2Cu_3O_7$	90
$TlBa_2Ca_2Cu_3O_9$	120
$Tl_2Ba_2Ca_2Cu_3O_{10}$	125

Table 1.1: Critical Temperatures of various superconductors

1.4.2 Critical Magnetic Field H_c

No matter what the temperature, a magnetic field larger than a certain value for a particular material causes the superconducting state to disappear. This value of the magnetic field is referred to as the superconductor's critical magnetic field.

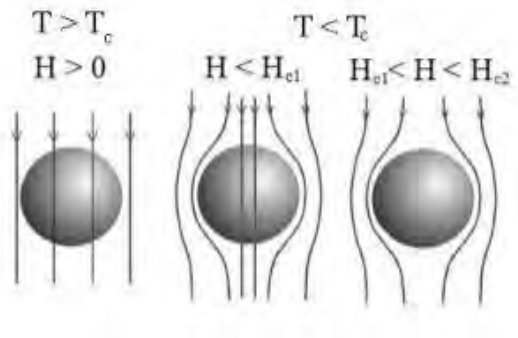

Fig 1.5: Expulsion of Magnetic field lines from the material when $T < T_c$ and $H > H_c$

If the applied magnetic field is increased while the material is in the superconducting state, the superconducting state cannot exist in a magnetic field greater than the material's critical magnetic field. H_c stands for the critical magnetic field. Eq (1.4) can be used to get the value of H_c at temperature T.

$$H_c(T) = H_c(0)\{1-\left(\frac{T}{Tc}\right)^2\} \qquad (1.4)$$

It is obvious that $H_c(T)$is the maximum critical magnetic field value that can exist at T=0. $H_c(T) = 0$ at $T = T_c$ indicates that superconductivity can be broken by a modest magnetic field at the critical temperature.

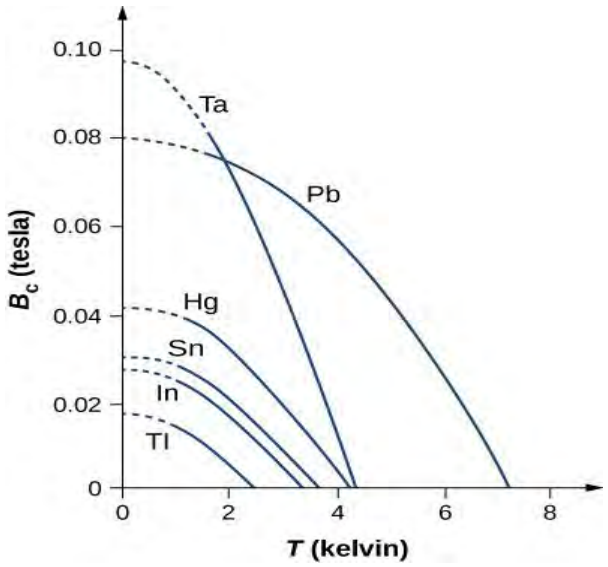

Fig 1.6: Temperature Vs Critical magnetic field for various superconductors

1.4.3 Critical current Density J_c

For large currents, a variety of superconducting thin wires are used to reduce resistance and energy losses. These tiny lines can only transmit a finite quantity of electricity. Kunzler first became aware of it in 1961. J_c depends on temperature, therefore if we place a superconductor in a colder environment, it will be more up to date.

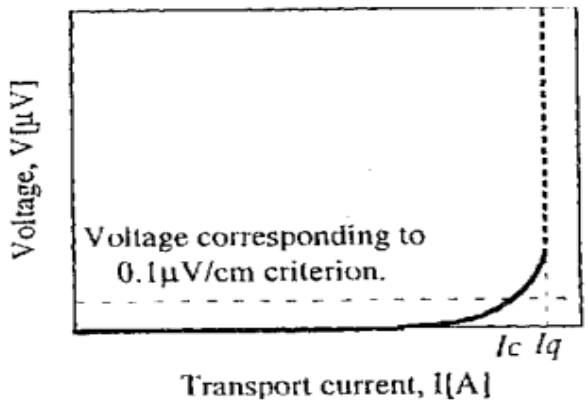

Fig 1.7: Voltage Vs Current graph for superconducting wire

1.4.4 Correlation between T_c, H_c & J_c

The three critical values are interdependent. At 0 Kelvin, J_c and H_c are at their maximum values. However, J_c and H_c become zero when the temperature reaches its critical value. A critical surface can be obtained from the plot of these three critical values. The substance inside this surface, it behaves as a superconductor, whereas the material would be in a normal state outside of it.

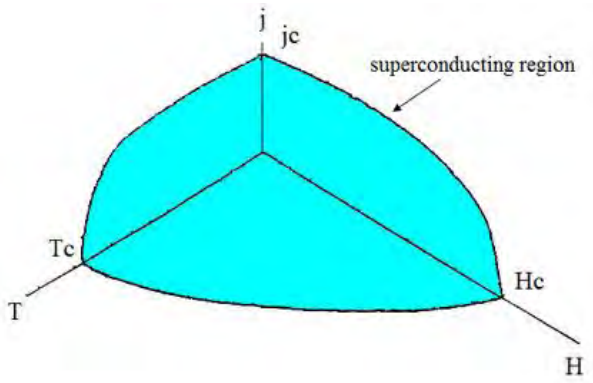

Fig 1.8: Critical Phase Diagram

1.5 Types of Superconductors

1.5.1 Type I Superconductors

Type I superconductors are those that show a sudden transition from a diamagnetic to a paramagnetic state at critical values of applied magnetic field. These superconductors strictly follow the Meissner effect, meaning that at all fields above the critical field, their magnetization is zero and they are perfectly diamagnetic. They are also known as soft superconductors. Because a relatively small critical field is needed to break the superconductivity of 27 superconductors. Type-1 superconductors Pb, Hg, and Sn have perfect diamagnetic behavior [6].

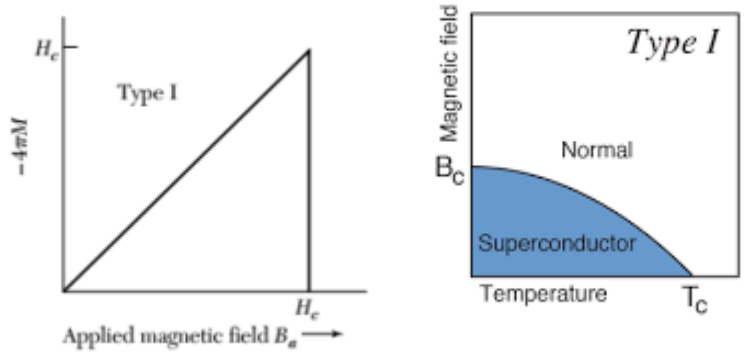

Fig 1.9: (a) Phase illustration of type-*I* Superconductor
(b) Magnetization Vs Applied Field of type-*I* Superconductor

1.5.2 Type II Superconductors

These superconductors do not obey the Meissner effect strictly and do not show a sudden transition from a diamagnetic to a paramagnetic state. When the specimen is in the lower critical field, or critical magnetic field "H_{c_1}," the magnetic flux cannot enters the specimen. In region $H < Hc_1$, the material shows perfect diamagnetic nature. Superconductivity slightly ruined between Hc_1 and Hc_2 (upper critical field). The region $Hc_1 < H < Hc_2$ is known as mixed or intermediate region. In the mixed region, magnetic flux penetrates in the form of vortices. Vortices distribute themselves equally in the material. In region $H > Hc_2$, magnetic field lines can penetrate in the material and as a result, superconductivity demolish. Supercurrent flows around the central core of each vortex as the magnetic field partially penetrate the mixed state in the form of a vortex. The field that enters the vortex has a tendency to be in opposition to the field coming from the specimen outside the vortex. Because a large magnetic field is required to demolish superconductivity, these superconductors are also known as hard superconductors. Type-II superconductors include Ni and metal alloys. [7]

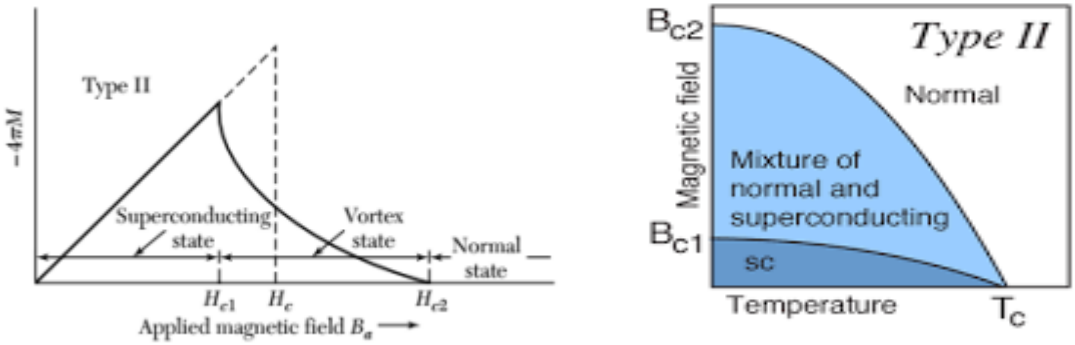

Fig 1.10: (a) Magnetization Vs Applied Field of type-*II* Superconductor
(b) Phase illustration of type-*II* Superconductor

1.6: Thermodynamic properties of Superconductors

1.6.1 Entropy

The measure of a state's disorderliness is called entropy. Because electrons in superconducting phases are more organized than those in normal phase. As a result, it shows that the normal state (S_N) entropy is higher than the superconducting state (S_S), although both states exist at the transition point (T_C) show same entropy [8]. The formula for the difference in entropy between these two phases is as follows:

$$S_N - S_S = -\frac{H_c}{4\Pi}\left(\frac{\partial}{\partial T}\right)_R \qquad (1.5)$$

Third law of thermodynamics states that at T=0 K, $S_N - S_S = 0$ as well.

$$S_N - S_S = 0$$

As

$H_C = 0$ at $T = T_C$

Additionally, $S_S < S_N$ implies that a superconducting phase is more ordered than a normal phase for $0 < T < T_c$, $(\frac{\partial}{\partial T} H_c) < 0$

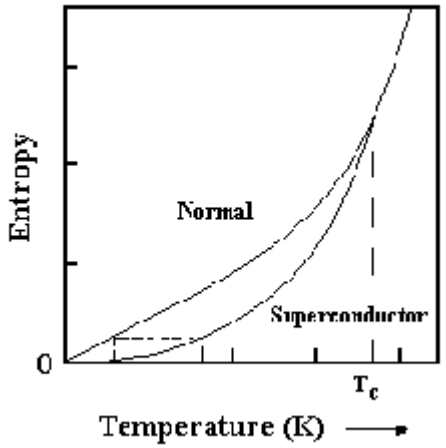

Fig 1.11: Entropy Vs Temperature

1.6.2 Specific Heat Capacity

Specific heat is the quantity of energy needed to raise an object's temperature by one degree Celsius per unit of mass.

Q = CmΔt is the formula for computing specific heat.

The specific heat of typical metals depends on temperature as follows:

$$C_n(T) = \gamma T + \beta T^3 \qquad (1.6)$$

A portion of the heat that is added to a system raises the electronic specific heat, which is shown by the first term. The second part in the equation above, which is used to represent the residual energy, is utilized to increase the lattice vibrations of the lattice at low temperature. Due to the fact that lattice features like crystal structure and Debye temperature are unaffected by superconductivity, including the pairing of electrons to create cooper pairs, specific heat due to lattice vibration is the same both in the superconducting state and the normal state. So, in this case, the electronic specific heat component will be our focus.

It has been discovered that the electronic specific heat component changes with temperature exponentially.

$$C_{es} = A \exp\left(\frac{\Delta}{k_B T}\right) \qquad (1.7)$$

where Δ stands for the energy gap. As the temperature drops below the transition point, this energy gap shrinks until it is zero. Additionally, this explains why superconductors' electrons have a higher specific heat than electrons in normal metals. However, the energy gap starts to widen more when the temperature is raised over that superconductor's critical temperature. This occurs along with the shattering of cooper pairs. Each electron needs an energy equivalent to the energy gap in order to split a pair. A cooper pair must be broken with two times the total energy or 2Δ.

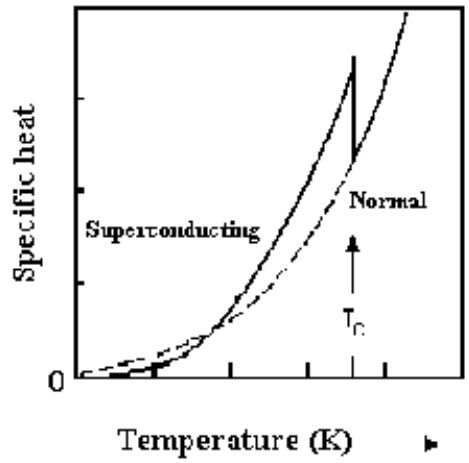

Fig 1.12: Specific Heat Vs Temperature

1.6.3 Free Energy

In thermal equilibrium, the Gibbs free energy is given by

$$G = \cup - TS - \frac{B \cdot H}{4\pi} + PV$$

Where;

U stands for total internal energy, S for entropy per unit volume, P for pressure, V for volume, and H and B for the magnetic field and flux, respectively, that have been applied.

$$F = U - TS \qquad \text{so;} \qquad G = F - \frac{B \cdot H}{4\pi} + PV$$

Helmholtz free energy is used to define F here [9]. The difference between the Helmholtz free energies of the superconducting state F_s and the normal state F_n is expressed as,

$$F_n - F_s = \frac{H_c^2}{8\pi} \qquad (1.8)$$

Condensation energy is another name for it, and H_c stands for thermodynamic critical field.

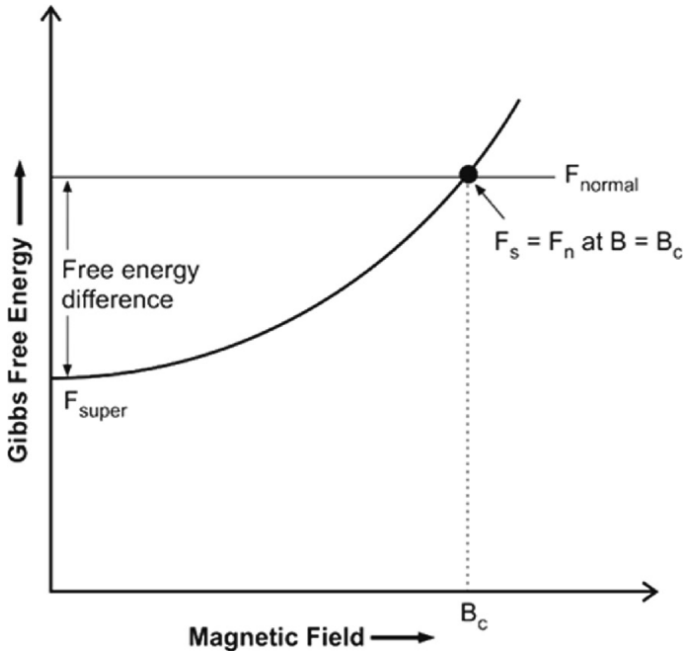

Fig 1.13: Free Energy Vs Magnetic Field

1.7 Dielectric Properties of Superconductors

Permittivity is a dielectric property. With various elements, such as temperature, frequency, pressure, and material structure, it alters in a superconducting sample.

1.7.1 Capacitor

A capacitor is a device for holding electrical charge. It is made up of an insulator sitting between two or more conductor layers. Charges accumulate and are stored in a capacitor when a voltage is applied across its plates, creating an electrostatic field. More charge can be stored because there is a dielectric between these plates.

C=Ad is the formula for a capacitor's capacitance.

Calculating the capacitance in farads (F).

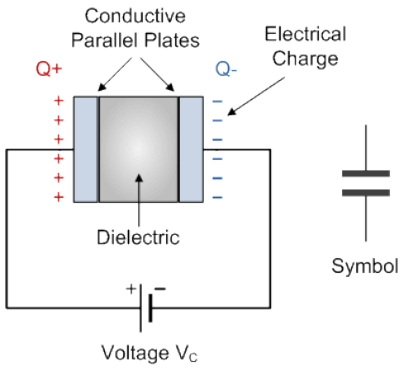

Fig 1.14: Parallel Plate Capacitor

1.7.2 Permittivity

When subjected to an applied electric field, a dielectric material has the capacity to store energy. When a parallel plate capacitor has a dielectric medium inside of it, the amount of charge stored increases [10]. The relation between capacitance and dielectric constant is;

$$C = \frac{\varepsilon_0 A}{d} \qquad (1.9)$$

Where $\varepsilon_0$represents the permittivity of empty space, A is the area of a parallel plate of the capacitor, d is the distance between them.

The electromagnetic theory of electric displacement or electric flux density D_f is

$$D_f = \varepsilon E \qquad (1.10)$$

$$\varepsilon = \varepsilon_0 \varepsilon_r \qquad (1.11)$$

Where ε_r is the relative permittivity and ε_0 is the permittivity of free space. A complex number called relative permittivity defines how an electric field interacts with a dielectric material.

The amount of energy that is stored in a material coming from an external field is indicated by its value (ε_r'). While the imaginary part (ε_r'') indicates the amount of field dissipation in the dielectric medium.

Whereas

$$\varepsilon_r' > \varepsilon_r''$$

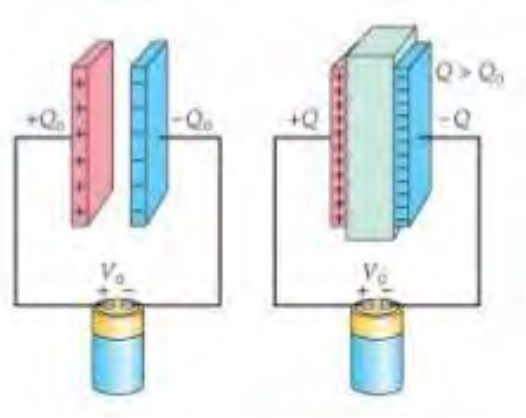

Fig 1.15: Parallel Plate Capacitor with or without Dielectric

1.7.3 Dielectric Loss ($\tan\delta$)

The ratio of the imaginary to the real parts of the dielectric constant is known as the loss factor.

$$\tan\delta = \frac{\varepsilon_r''}{\varepsilon_r'} \qquad (1.12)$$

The term "dissipation factor" or "tan delta" are other names for it.

1.8 Theories Explaining the phenomenon of Superconductivity

1.8.1 London Theory:

In 1935, two brothers named Heinz and Fritz London developed a theory to account for the Meissner effect. They divided all of the electrons in superconducting samples into two categories using two fluid models: normal electrons (n_n) and superconducting electrons (n_s), resulting in $n = n_n + n_s$ as the final density. The most superconducting electrons would be present as the temperature got close to its critical point $T \to T_C$.

Because $T \to T_c$ and $n_n \to 0$, n_s →maximum for $T < T_C$

As

$T \to T_C$, $n_s \to 0$, n_n → maximum for $T > T_c$

Consider a uniformly applied electromagnetic field to the superconducting sample. Both fields are thought to be so weak that superconducting electrons are unaffected by them. If V_s is the average

velocity of super electrons, m is its mass, and e is its charge, then the equation of motion in the presence of the electromagnetic field E.

$$m\left(\frac{dv_s}{dt}\right) = -eE \tag{1.13}$$

The following formula is used to compute the current density of superconducting electrons:

$$J_s = -en_sV_s$$

$$\frac{dJ_s}{dt} = \frac{n_se^2E}{m} \tag{1.14}$$

Because it shows that steady state current J_s remains constant in the absence of an electric field, it is known as the first London equation. While $J_n = \sigma E$ is the current density of ordinary electrons, demonstrates that E=0, which is consistent with the common situation. Here is the Maxwell equation:

$$\nabla \times E = -\frac{dB}{dt} \tag{1.15}$$

As E=0 means that B is constant, Meissner's effect cannot exist since the magnetic field inside the superconductor is not uniform. London suggested altering the statement [11] to remove this inconsistency, which is

$$\nabla \times J_s = -\frac{n_se^2B}{m} \tag{1.16}$$

The result also referred to as the London second equation, is compatible with the experiment.

1.8.1.1 London Penetration Depth (λ)

By creating a permanent supercurrent on its surface, a superconductor expels the external magnetic field by creating a magnetic field that opposes the applied field and cancels it out. This supercurrent circulates in a thin layer of thickness λ, is determined by the subsequent relationship, penetration depth.

$$\lambda = \left(\frac{m^*C^2}{4\pi n_se^2}\right) \tag{1.17}$$

Where n_s is the density of superconducting electrons and m* is the effective mass of carriers.

The relationship between penetration depth and temperature is linear.

$$\lambda(T) \sim \frac{\lambda(0)}{\left[1-\left(\frac{T}{Tc}\right)^4\right]^{\frac{1}{2}}} \qquad (1.18)$$

London penetration depth is another name for this substance, which was created by the London brothers.

Eq. 1.15 relates it to the coherence length

$$k = \frac{\lambda}{\xi GL}$$

Where;

$$\xi_{GL} = 0.74\xi_0 \left(1 - \frac{T}{T_c}\right)^{-1/2} \qquad (1.19)$$

Ginzburg-Landau parameter k is used here. This parameter describes the superconductor and is unaffected by temperatures around the critical temperature (T_C) [12].

1.8.2 BCS Theory:

The first microscopic theory to be proposed was the BCS theory by Bardeen, Cooper, and Schrieffer in 1957 [13]. Leon Cooper first proposed the concept of electrons interacting in an attractive way to form a pair known as the Cooper pair. The phonons or lattice vibrations work as a mediator to cause the electrons to attract one another. The electron attracts the positive ions that make up a lattice but repels other electrons because of their negative charges. Yet, when an electron passes over positive ions, it distorts the lattice from the mean position via attractive potential, raising the positive charge density nearby. An additional electron is attracted by the positive charge density. The attraction between electrons can overcome their repulsion due to the displaced ion and force them to form a pair. Due to their attractive potential, the pair of electrons produced via electron phonon interaction behave like composite bosons. At $T_c(R = 0)$, these composite bosons, known as Cooper pairs, condensed to form the ground state and followed the Bose-Einstein statistical model.

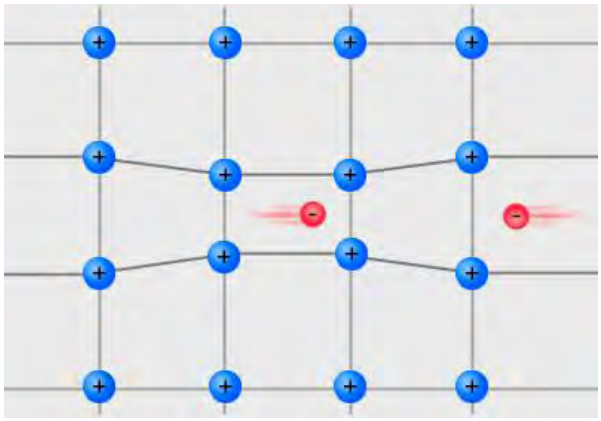

Fig 1.16: Formation of Cooper Pair

The Cooper pair was created in momentum space when one electron emitted a phonon with momentum $\hbar q$ and the other electron absorbed it.

This interaction is given by;

$$V_{eff} = \left|g_{eff}\right| \frac{1}{\omega^2 - \omega_D^2} \qquad (1.20)$$

Here, ω the frequency of the electron under consideration, ω_D is the Debye frequency, and $\left|g_{eff}\right|$ is the matrix element describing the probability of one electron generating a virtual phonon and another electron absorbing it. When electrons at the fermi level participate in attraction and their energies above the fermi level are less than or equal to the Debye energy of the lattice ($\hbar\omega_D$), this is known as the negative V_{eff} which stands for attractive potential.

The cooper pair's attractive interaction results in a bound state with the mathematical equation for energy given by;

$$|E| = 2\hbar\omega_D \, e^{N(E_f)} \Big/ g_{eff} \approx 1.76 k_\beta T_C \qquad (1.21)$$

Here, the critical temperature T_c, the Boltzmann constant k_β, and the density of electron states at the fermi level $N(E_f)$. For the weak coupling limit, the value of 1.76 is accurate and is valid for most but not all typical superconductors.

The band gap appeared at critical temperature T_c(R=0) due to the formation of condensation state having energy less than the normal state. A bridge between the normal and superconducting states

is created by the band gap. In the case of low temperature superconductors, the band gap's decreasing dependency on temperature was successfully predicted. This theory holds true for conventional superconductors, which have s-wave symmetric band gaps and linear interactions between electrons and lattice vibrations (phonons). Yet, in an unconventional superconductor, the interaction becomes nonlinear due to a strongly correlated medium, where each carrier's position and dynamics have a significant impact on every other carrier. Moreover, appearance of psedogap in a normal state of superconductor is a mystery for BCS theory.

1.8.3 The Ginzburg-Landau Theory (GL):

The first quantum theory of superconductivity was published by V. L. Ginzburg and L. D. Landau in 1950[14]. The London hypothesis did not account for the quantum effect. But there was a clear need for quantum theory. Firstly, the entropy of the superconducting state is less than the normal state, Secondly, a second order phase transition occurs when a material changes from its normal state to its superconducting state, it inspired the concept of an order parameter Ψ. The complex wavefunction, which is non-zero for a $T < T_C$ and zero for a $T > T_C$. Superconducting electrons serves as the order parameter in this system. GL theory, based on the second order phase transition of the Landau theory. This theory is based on the free energy expansion with regard to the small power order parameter Ψ at the transition temperature.

Because $T - T_C << T_C$, this theory is true close to the critical temperature. The normalized version of the order parameter, $|\Psi|^2$, which provides the density of superconducting electrons, was used in the formulation of the theory.

$$|\Psi|^2 = \frac{n_s}{2} \qquad (1.22)$$

where "n_s" denotes the density of superconducting electrons.

Furthermore, they made assumption that a Ψ doesn't depend on position r, i.e., that no external field is applied that would make a Ψposition dependent.

The expansion of free energy mathematically written as;

$$F = F_n + \alpha|\Psi|^2 + \frac{\beta}{2}|\Psi|^4 \qquad (1.23)$$

Here, α and β are the phenomenological expansion coefficients that depend on the superconducting material, and F is the free energy density and F_n is the free energy density in the normal state. The expansion of free energy will be caused by the application of a magnetic field (B).

$$F = F_n + \alpha|\Psi|^2 + \frac{\beta}{2}|\Psi|^4 + \frac{1}{2m^*}|(-i\hbar\nabla - 2e^*A)\Psi|^2 + \frac{|B|^2}{2u_0} \quad (1.24)$$

The vector potential in this case is A.

After reducing the above equation, we obtain two generalized GL theory equations, i-e

$$\alpha\Psi + \beta|\Psi|^2\Psi + \frac{1}{2m^*}\left(-i\hbar\nabla - \frac{e^*}{C}A\right)^2\Psi = 0$$

$$J_S = \frac{i\hbar e}{2m^*}(\Psi^*\nabla\Psi - \Psi\nabla\Psi^*) - \frac{2e^2}{mc}|\Psi|^2A \quad (1.25)$$

Here are two particular lengths of a Ginzburg-Landau theory: coherence length $\xi$and penetration depth λ.

$$\xi = \sqrt{\frac{\hbar^2}{2m|\alpha|}} \quad (1.26)$$

$$\lambda = \sqrt{\frac{m}{4e^2\Psi u_0}} \quad (1.27)$$

The coherence length denotes the thermal fluctuation or order parameter length, and λ denotes the magnetic field's (B) depth of penetration at a superconducting material's surface. Ginzburg-Landau present a new parameter "κ" known as the GL parameter, which is defined as

$$k = \frac{\xi}{\lambda} \quad (1.28)$$

Where;

$|\Psi|^2 = 1$ in superconducting state and $|\Psi|^2 = 0$ in normal state.

1.8.3.1 Coherence Length (ξ):

Electrons (with opposite spins) may not actually come close to one another during the creation of a cooper pair. Their contact covers a large area (order of hundred nanometers). Hence, even when

they are far apart, they continue to exist as a pair. Coherence length (ξ) is the term used to describe the typical separation [15] between two electrons in the paired state of cooper pair. Compared to high temperature superconductors, it has a higher value for low temperature superconductors.

According to BCS theory;

$$\xi = \frac{\hbar V_F}{2\Delta} \qquad (1.29)$$

Fermi velocity is defined as V_F and the energy gap is 2Δ.

If $\xi > \lambda_L$; it indicates type-I superconductor

If $\xi < \lambda_L$; it indicates type-II superconductor

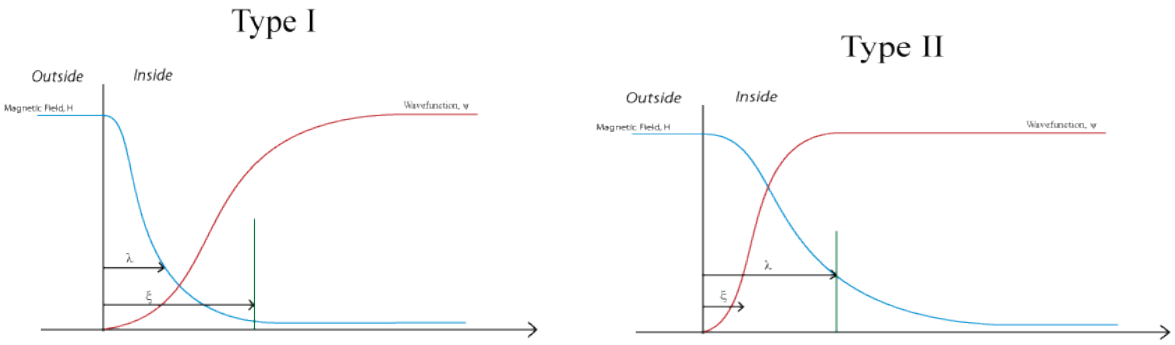

Fig 1.17: Classification of Superconductors on basis of GL-Parameter

1.9 Magnetic Flux Quantization

The flux quantization phenomena can be used to demonstrate the quantum character of superconducting state. As we have studied, the entire magnetic field is ejected from a superconductor when it is placed in a magnetic field and cooled to its T_c. Flux may become trapped in the superconductor's hole if one exists. The flux trapped in the hole has been empirically proven to be an integral multiple of the quantity ϕ_0, where ϕ_0 is defined as

$$\phi_0 = \frac{\pi\hbar c}{e}$$

$$\phi = n\phi_0 \qquad (1.30)$$

Where the flux trapped in the superconductor hole is denoted by the symbol ϕ and c represents the speed of light in a vacuum. This demonstrates the quantization of the flux trapped in the hole [16]. If this magnetic flux is quantized then the current flowing around the hole must also be quantized.

1.10 Isotopic effect

In 1950, H. Frohlich made the first hypothesis on the role of mass in the process of superconductivity. He suggested that important aspect of the superconducting action is played by the material's pulsing atoms [17]. Based on the hypothesis of H. Frohlich, E. Maxwell and C. A. Reynolds discovered the isotope effect in the same year. They studied different mercury isotopes and discovered the relationship between Tc and isotope mass as follows:

$$T_C M^{\alpha} = constant \qquad (1.31)$$

This analysis revealed that the critical temperature varies with the mass of the isotopes of the superconducting element [18, 19].

1.11 Josephson Effect

The current value that can be expected to flow when tunnelling of Cooper pairs up to few nanometers happens, over a thin insulating barrier linked (sandwiched) in two superconductors, was computed by B. D. Josephson in 1962[11]. (Josephson junction). He gave the initial theoretical account of quantum-mechanical tunnelling. This theoretical explanation at the macroscopic scale was experimentally confirmed in 1963 and is known as the Josephson's effect. Along with Leo Esaki and Ivar Giaever, who conducted experimental investigations into the tunnelling phenomenon in semiconductors and superconductors, respectively.

There are two versions of the Josephson Effect:

- the Dc Josephson effect.
- the Ac Josephson effect.

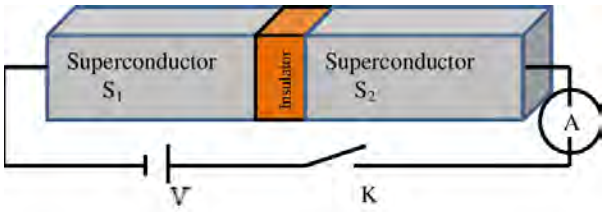

Fig 1.18: Josephson Junction

1.11.1 DC Josephson Effect:

Cooper pair flow is essentially a supercurrent. Without using any external voltage, the current travels through the weak link in this form of Josephson effect. The reason for this current flow (at zero bias) is cooper pair tunnelling. These Cooper pairs' wave functions penetrate the insulating (linking) layer and are phase-sealed together [21,22]. Because of this, the insulating layer can conduct current at zero voltage, which is known as the DC Josephson effect.

1.11.2 AC Josephson Effect

In ac Josephson effects, a finite voltage V applied across the barrier causes a change in phase over time. Moreover, the current oscillates between the two superconductors with a frequency ω that is linked to the applied voltage ($\hbar\omega = 2eV$), causing a change in phase. Hence, instead of the DC Josephson effect, we will see something else. The ac Josephson Effect is the continuous flow of current that occurs when Cooper pairs quantum tunnel across a junction at a finite (fixed) voltage.

1.11.3 Josephson Tunneling Effect

Let's imagine a thin insulating barrier between two superconductors.

Assume that the wave functions are Ψ_1 and Ψ_2. Coupled Schrodinger wave equations are used to

$$i\hbar\frac{\partial\psi_1}{\partial t} = \mu_1\psi_1 + k\psi_2 \qquad (1.32)$$

$$i\hbar\frac{\partial\psi_2}{\partial t} = \mu_2\psi_2 + k\psi_1 \qquad (1.33)$$

where K Coupling constant and,$\mu_1$and μ_2 are superconductor's lowest energy states.

Let's say that the wave functions are defined as:

$$\psi_1 = (n_1)^{1/2}e^{i\theta_1}$$

$$\psi_2 = (n_2)^{1/2} e^{i\theta_2}$$

Here, the phases are $\theta_1 and\ \theta_2$ while the number densities are n_1 and n_2. When we enter values for ψ_1 and ψ_2 into Eqs. (1.32) and (1.33), we obtain,

$$\hbar \frac{\partial n_1}{\partial t} = -\hbar \frac{\partial n_2}{\partial t} = 2k(n_1 n_2)^{1/2} \sin(\theta_2 - \theta_1) \qquad (1.34)$$

$$\hbar \frac{\partial(\theta_2 - \theta_1)}{\partial t} = \mu_2 - \mu_1 \qquad (1.35)$$

$I = \frac{\partial n}{\partial t}$, because the rate of change in number density. The levels with the lowest energy will have a voltage V applied to the Josephson junction, which will result in levels with = 2eV. Eventually, Josephson junction equations will,

$$I = I_0 \sin \delta \qquad (1.36)$$

Where,

$$I_0 = \frac{2k(n_1 n_2)^{1/2}}{\hbar} \quad \& \quad \delta = \theta_2 - \theta_1$$

$$\frac{\partial \delta}{\partial t} = \frac{2ev}{\hbar} \qquad (1.37)$$

1.12 Applications of Superconductors

Superconductors are used in a wide variety of businesses and academic research. Here are some examples of superconductor applications.

1) The following uses of superconductors are based on the notion of zero resistance.

- With no power loss in power transmitting lines
- Electric generators and particle accelerators use superconducting magnets.

2) Utilizing the 'Meisner Effect,' a famous property of superconductors, superconductors are used for the following purposes.

- Magnetic Protection
- Imaging with magnetic resonance (MRI)

- Trains using magnetic levitation

3) The following applications of superconductors are based on Josephson impact.

- Magneto cardiogram during mineral exploration
- Detectors of magnetic flux
- Rapid computer systems
- Devices with superconducting quantum interference (SQUIDS) Logic components
- Aeroplane and computer chip evolution without causing harm [23]

References

[1] R. Simon and A. Smith, Superconductors: Conquering Technology's New Frontier, Plenum, New York, (1988)

[2] I.A.C Rose and E.H. Rhoderick, Introduction to Superconductivity, Pergamon Press, (1969).

[3] V.V. Schmidt, (Eds) Paul Muller and Alexey V. Ustinov, The Physics of Superconductors, (1997).

[4] Andrei Marouchkine, Room Temperature Superconductivity, Cambridge International Science Publishing, (2004).

[5] Meissner, W. and R. Ochsenfeld, Ein neuer effekt bei eintritt der supraleitfähigkeit Naturwissenschaften, 1933. 21(44): p. 787-788.

[6] Z.Z. Sheng, A.M. Hermann, Nature 332 (1988) 138–139.

[7] T.W. HUANG, M.P. HUNG, T.S. CHIN, H.C. KU, S.E. HSU, Mod. Phys. Lett. B 04

[8] H. Froehlich,: Physical Review, 79 (1950) 845-856. (2004) 885–893.

[9] A.P. Drozdov, M.I. Eremets, I.A. Troyan, V. Ksenofontov, S.I. Shylin, Nature 525 (2015) 73–76.

[10] M.A. Wahab, Solid State Physics, Narosa Publishing House Pvt. Ltd, New Delhi, 2nd edition.

[11] London, H. and F. London, Proc. Roy. Soc. Lond., Ser. A, 1935. 149: p. 71.

[12] Mourachkine, A., Room-temperature superconductivity. 2004: Cambridge Int Science Publishing.

[13] J. Bardeen, L.N. Cooper, J.R. Schrieffer, Phys. Rev. 108 (1957) 1175–1204.

[14] N.A. Khan, A. Saba, A. Raza, J. Alloys Compd. 757 (2018) 476–483.

[15] S.O.Pillai, Solid State Physics, 5th Edition, New Age International (p) Limited Publishers (2002).

[16] Doll, R. and M. Näbauer, Experimental proof of magnetic flux quantization in a

superconducting ring. Physical Review Letters, 1961. 7(2): p. 51.

[17] Norman, M., A magnetic isotope effect. Nature Physics, 2006. 2(1): p. 19-20.

[18] Conder, K., Oxygen diffusion in the superconductors of the YBaCuO family: isotope exchange measurements and models.

Materials Science and Engineering: R: Reports, 2001. 32(2-3): p. 41-102.

[19] Soerensen, G. and S. Gygax, Evaluation of oxygen isotope experiments on Pr-, Ca-, and Zn-substituted ${\mathrm{YBa}}_{2}$${\mathrm{Cu}}_{3}$${\mathrm{O}}_{7}$. Physical Review B, 1995. 51(17): p. 11848-11859.

[20] B.D. Josephson, Phys. Lett. 1 (1962) 251–253.

[21] josephson, B. D., "Possible new effects in superconductive tunnelling," Physics

Letters 1(1962) 251.

[22] Josephson, B. D.: Rev. Mod. Phys. 46 (2) (1974)251–254.

[23] Knauss, L.A., et al., Scanning SQUID microscopy for current imaging. Microelectronics Reliability, 2001. **41**(8): p. 1211-1229.

Chapter No: 02

Literature Review

The influence of magnesium replacement for superconducting and structural properties has been investigated in a large number of samples in various superconductive systems. Here, a brief review of the work done so for on the substitution of Mg in HTSCs is presented.

2.1 Review of High Temperature Superconductors (HTSCS)

K. Konstantinov and S. Karbanov et al. [1] examined the magnesium's effects on samples from the Bi-Mg-Sr-Ca-Cu-O system's superconducting properties and phase composition is investigated. X-ray diffraction and temperature-dependent measurements of electrical resistance used to study the synthesized materials. In the monophase 2212 sample, Tc is equal to 88 K. Tc values for the nominal compositions $Bi_{1.6}Mg_{0.4}Sr_2Ca_2Cu_3O_y$ and $Bi_2Mg_1Sr_2Ca_2Cu_3O_y$ are 94.5 K and 93 K, respectively. According to the conclusions of the X-ray phase study, adding magnesium to Bi-Sr-Ca-Cu-O causes emergence of the 2212 phase, which predominate, the 15 K phase $Bi_2Sr_2Ca_2Cu_lO_6$ (2201), as well as minor amount of unreacted CuO. A few more faint lines are seen; these are almost certainly satellite peaks of basic-phase peaks. The value of Tc does not match the optimal phase composition, according to a comparison of the electrical measurements and the results of the X-ray phase analysis. Tc should decrease to values that are less than those of the monophase 2212 sample due to the presence of the 2201 phase and CuO in the Mg-containing components. However, the results reveal that the Mg-doped materials have critical temperature is approximately 6 K higher.

S. Mazumder et al. [2] proposed the effects of doping $YBa_2Cu_3O_7$-δ with Mg on its crystalline structure and superconducting behaviour have been examined. A neutron diffraction pattern showed the sample's orthorhombic (Pmmm) symmetry. Even at the highest Mg concentration, the cell constants basically remain unchanged, with the exception of an initial marginal drop. The ionic radius of Mg^{2+} is 0.57 A^o, which is noticeably lower than that of Cu^{2+}, which is 0.73 A^o. As x (concentration) rises, T drops very rapidly and almost linearly. Above 4.2 K, the sample with x=0.36 does not superconduct.

Nawazish A. Khan et al. [3] investigated the superconducting characteristics of Cu_{1-x} Tl_x Ba_2 Ca_{3-y} Mg_y $Cu_4O_{12-\delta}$ (Cu_{1-x} Tl_x Mg_y -1234) in the composition range y = 0, 1.5, 2.25. The samples with and without Mg doping exhibit normal state metallic resistivity that depends on temperature. The samples with y=0, exhibit zero resistance at 121 K and superconductivity begins at 136 K.. The samples' critical temperature for zero resistance is 131 K, while their superconductivity begins at 143 K. Value of T_C for $Cu_{1-x}Tl_x$ -1234 superconductors is now the highest yet observed. Samples with Mg substitution have a higher $T_C(R=0)$ due to the shorter c axis length and improved interplanar coupling. The material's critical temperature may increase as a result of the shortened c axis, which may increase the carriers' Fermi-velocities along-c axis . According to the XRD pattern, the lattice parameters for the Mg-free samples were a=3.917 A^o and c=18.126 A^o after the peaks were fitted to the tetragonal structure. On the other hand, the Mg substitution resulted in a significant shortening of the axis a and c. Sample which have Mg concentration of y=1.5, the lattice parameters were a=3.899A^o and c=18.102A^o, while in the sample with y=2.25, they were a=3.897A^o and c=18.081A^o. Mg replacement at the Ca site may be most probable cause of the shortening of a and c axes' lengths in the samples with Mg doping. Mg shortens c axis of the $Cu_{1-x}Tl_x$ ($Cu_{1-x}Tl_x$ Ba_2 Ca_3 Cu_4 $O_{12-\delta}$) unit cell due to its smaller ionic radius than the Ca ion. The reduced c axis shows higher interplane interaction as well.

Nawazish A. Khan et al. [4] inquired by using a para-conductivity analysis approach, one can determine how the characteristics of Tl Ba_2 $(Ca_{3-y}Mg_y)Cu_4O_{12-\delta}$ (y = 0-2.0) superconducting alloys are affected by the addition of magnesium. The samples were made using the solid-state reaction approach, which involved applying the proper pressure before annealing them at 500^{o}C. The samples' Tc(offset) and Tc(onset) values increased up to y = 1. Excess conductivity analysis showed that increasing Mg content in the samples increased the values of inter-planar coupling J and coherence length $\xi c(0)$ because it decreased the order parameter of charge carriers in CuO_2 planes. $B_{c1}(T)$, $B_{c0}(T)$, and $J_c(0)$ parameters decreased because the addition of magnesium at calcium positions in the unit cell reduced intensity of inter-grain interaction.

N. Khan et al. [5-6] conceived an idea of a Mg/Be substitution in various ratios at the Ca site in $(Cu_{0.5}Tl_{0.5})Ba_2Ca_2Cu_3O_{10-\delta}$. They used CuCN, MgO, $Ca(NO_3)_2$, and $Ba(NO_3)_2$ as the parent compounds in the synthesis of $(Cu_{0.5}Tl_{0.5})Ba_2Ca_2Cu_3O_{10-\delta}$ (where x = 0, 0.5, 1, and 1.5). The solid state reaction method was used to properly grind these compounds for an hour, and then they were

burned in quartz boats at 840°C. After the initial firing, they are again grind, and the sample is saved for the subsequent firing in the furnace. At the end, Tl_2O_3 was mixed through grinding to create the final compound, $Cu_{0.5}Tl_{0.5}Ba_2Ca_{2-x}Mg_xCu_3O_{10-\delta}$, where x = 0, 0.5, 1, and 1.5. The resulting composite was sintered for 10 minutes inside a pelletized aluminium foil. They notice a consistent pattern of raising T_c in response to Ca doping at various ratios. They discovered that for x = 0 composition, measured T_c(R =0) was 82 K, and for x = 1.5, it was 92 K after performing four probe resistivity measurements. They draw the conclusion from their findings that higher Tc(R=0) values result from the doping of more electronegative Mg at less electronegative Ca sites, which causes the displacement of Cu electron clouds towards Mg and may be a possible reason of the shortening of the c axis length, as shown by the XRD analysis.

S.K. Agarwal et al. [7] Reported $Cu_1Ba_2Ca_3Cu_4O_{12-\delta}$, which is doped with Mg at Ca sites and synthesised at 3.5GPa pressure and 1000°C temperature, is being studied as a superconducting sample. Measurements of the Hall effect, four probe resistivity, and XRD analyses were used to characterize these samples. The lattice parameters a-axis and c-axis were found to be reduced by the increase Mg concentration at Ca sites. When the Mg content at Ca sites is raised, the holes concentration (n_h) in the Hall measurements decreases. Furthermore, they carried out critical-field measurements, reporting that aligned samples had anisotropy in the c-axis that was greater to that of the original Cu-1234 material. They observed such a small degree of anisotropy because the concentration of holes has reduced in the charge carrier block. The decrease in the inter-superconducting $Ca_3Cu_4O_8$ block's spacing is most likely caused by the reduction in the concentration of holes, which also lowers the c-axis.

Kashif Naseem et al [8] Study that in high-temperature superconductors, the charge transfer procedure requires the charge reservoir layer.. The impact of changing Ba atom in the $Cu_{0.5}Tl_{0.5}$-1223 crystal to a Mg atom on the $Cu_{0.5}Tl_{0.5}Ba_2O_{4-\delta}$ charge reservoir thickness has been examined. By means of a two-step solid-state reaction procedure, $Cu_{0.5}Tl_{0.5}(Ba_2\text{-}xMg_x)Ca_2Cu_3O_y$ (x = 0, 0.15, 0.25, 0.35) samples of a superconductor were produced. XRD results show that, with the exception of the peaks observed at around 2θ = 30° and 34° caused by an excess of unreacted $BaCuO_2$ impurity, a frequent occurrence in CuTl-1223phase, the PMMM space group's orthorhombic crystal structure can be used to match the majority of the diffraction lines. The final compound's a- and b-axis lengths reduced as Mg was added in increasing amounts. When the amount of

magnesium doping in the end product rises, it was also seen that samples showed c-axis length and unit cell volume suppression. Thus, it appears lower atomic size of Mg compared to Ba promotes suppression of the c-axis length and unit cell volume. From room temperature to 77 K, the samples' conductivity $\rho_{(T)}$ was measured. These samples were found to typically exhibit a metallic fluctuation of resistivity to the emergence of superconductivity at low temperatures. With the Mg doping content in end compound, resistivity of the samples at room temperature increased. With Tc(R = 0) values of 104K, 103K, 99K, and 103K, respectively, the beginning of superconductivity in the samples was noted at about 110K, 109K. When Mg was doped at the Ba site, excess conductivity measurements revealed an increase in ξc(0), ν_F, $\lambda_{p.d(0)}$, and interlayer coupling. This rise was most likely caused by the drop in the sample's superconducting volume proportion. From the charge reservoir layer to the conducting planes, the process for transferring charge carriers becomes increasingly effective. However, it was discovered that the density of pinning centers was decreased with increased Mg doping in the final compound by the suppression of parameters such $B_{c0}(T)$, $B_{c1}(T)$, $J_{c0}(0)$, and τ_{ϕ}.

Nawazish A. Khan et al [9] Studied that in $Cu_{1-x}Tl_xBa_2Ca_2Cu_{3-y}Ni_yO_{10-}\delta$ (y = 0, 0.5, 1.0, 1.5) superconductors, Ni doping has not been found to significantly reduce superconductivity. To observe the impact of improved the interactions of the nickel ions with the mobile carriers in the planes. Mg substituted at the Ca position in $Cu_{1-x}Tl_xBa_2Ca_{2-y}Mg_yCu_{1.5}Ni_{1.5}O_{10-}\delta$ superconductors (y = 0, 0.5, 1.0, and 1.5). XRD measurements shows that with the rise in Mg content in the unit cell, the length of a and c-axes increases. In $Cu_{1-x}Tl_xBa_2Ca_2$-$yCu_{1.5}Ni_{1.5}O_{10-}\delta$ superconductors, with the increase in magnesium doping, the zero resistivity critical temperature and the magnitude of diamagnetism. Li doping in the $(Cu_{0.5}Tl_{0.5})Ba_2O_{4-}\delta$ charge reservoir layer and post-annealing the samples in an oxygen atmosphere both further improve these parameters (the critical temperature and magnitude of diamagnetism). With the increased concentration of Mg, the FTIR absorption measurements have revealed a hardness of the apical oxygen mode between 485 and 497 cm^{-1}. Li doping softens these modes in both Mg free and Mg doped samples, which is most likely the result of optimized carrier concentration in conducting CuO_2/NiO_2 planes.

2.2 Review of Magneto Resistivity

R Awad et al [10] used the Solid-state reaction approach to produce superconductors with composition $TlBa_2Ca_{2-x}Sc_xCu_3O_{9-}\delta$ with x = 0.0, 0.025, 0.05, 0.1, and 0.2. To better understand

the phase-specific flux motion, prepared sample's electrical resistivity under weak magnetic fields as much as 4.4 KG has been investigated. Results show that as magnetic fields increase, critical temperature shifts slightly and the width of the superconducting transition ΔT, rises. These outcomes are simply result of the fact that, at low temperatures (T_c), there is very little difference between the resistivity of ordinary materials and superconductors. This indicates that the carriers are not all superconducting, only a small fraction of them. Such behavior might be explained by the high energy called intragrain pinning stops any vortex motion close to T_c. A resistivity tail arises as the temperature reduces because the electrical resistivity becomes more sensitive to the magnetic field that is being applied. This indicates increasing number of superconducting carriers at lower temperatures, which causes a larger change in resistivity with regard to the applied field and the zero field or related to weak links between the grains. The fluctuation of flux pinning activation energy with the applied magnetic fields is examined. When magnetic fields that are present are increased to 1.1 KG, U(B) reduces rapidly until it reaches a practically plateaued value at 4.4 KG. A power law relation is used to fit the data, with $U(B) \sim B^{-\beta}$. It is evident as x rises from 0 to 0.05, U(B) initially increases and then falls. Based on how the width of transition ΔT affected by the magnetic field, one can derive temperature dependence of U. Investigation is also done into how much the transition width ($\Delta T = T_c - T_0$) varies when there is magnetic field. The scaling relationship of power law as $\Delta T \alpha B^n$ is good fit for the transition width data.

Palstra, T.M., et al [11] examined that below T_c all temperatures and for all magnetic fields greater than H_{c1}, a new dissipation behavior in superconductor $Bi_{2.2}Sr_2Ca_{0.8}Cu_20_{8+}\delta$ is presented. The thermally activated current-independent electrical resistivity can be explained by an Arrhenius law and an activation energy $U_o(H,\phi)$ that is affected by the magnetic field and orientation. Enormous magnetoresistance is clearly seen at temperatures that are relatively low when temperature dependence of electrical resistivity, $\rho(T)$, is examined three parallel fields and one perpendicular field to the basal (a, b) plane for zero field. The I-V curves' linearity for temperatures between 10 and 80 K and currents between 0.1 and 100 mA in a field of 1 T reveals that linearity deviations begin to appear above 30 mA. When magnetic fields either parallel or perpendicular to the basal plane, the "onset" of resistivity can be observed. Thermally activated behavior of the resistance is apparent on the Arrhenius plot of $H \perp (a, b)$ as logp vs. T^{-1}. The activation energy $U_o(H,\phi)$ is represented by the curves' slope. The activation energies for H(parallel) and H(perpendicular) are

relatively small, with values ranging between 300 and 3000K, according to the dependence of the activation energy on the magnetic field.

H. Abbasi et al. [12] in different weight fractions, $MgCO_3$ particles were added to the powder of $Bi_{1.66}Pb_{.34}Sr_2Ca_2Cu_3O_{10+}$. Bi2223/MgCO3 powder was processed using a conventional solid state reaction procedure to yield bulk samples. X-ray diffraction and magneto resistivity have been used to examine the superconducting characteristics of materials for various $MgCO_3$ concentrations. There are two phases, high-T_C Bi2223 phase and low-T_C Bi2212 phase, according to studies using X-ray diffraction at room temperature. Orthorhombic Bi2223 ($Bi_{1.66}Pb_{.34}Sr_2Ca_{2-x}Mg_xCu_3O_y$) phase is the dominant phase in every sample, with a few orthorhombic Bi2212 phase peaks also present. The XRD data showed that, with increasing $MgCO_3$ addition, the intensities of peaks corresponding to the Bi2223 phase decreased while those belonging to the Bi2212 phase increased. When $MgCO_3$ is increased, the c-axis's length decreases, however, the a (and/or b) axis remains unchanged significantly. Measurements of magneto resistivity were performed in various DC magnetic fields (0, 0.3, and 0.6 T). The samples' normal state resistivity doesn't change much as the applied magnetic field increases. The resistivity transition width, however does grow with the addition of MgCO3 and an increase in the applied magnetic field. The degree or strength of the pinning force is inversely proportional to the extent of the broadening and shift of T_C (R= 0) towards lower temperature as a function of the magnetic field. The lesser critical current, weaker the pinning effect. For high T_C superconductors, the effective activation energy plays a key role in the description of flux dynamics in the mixed state. It has been discovered that the tail portion of resistivity follows the Arrhenius relation as stated by $\rho(H,T) = \rho_0 \exp(\frac{-U(H)}{k_B T})$; the slope of Arrhenius graph can be used to estimate the U value. Activation energy plot determine the flux pinning energy for each sample reduces as the applied magnetic field is increased. This also demonstrates decrease in flux pinning energy as the $MgCO_3$ doping level in the Bi2223 system increases.

Shakil Ahmad et al. [13] studied that thermally activated flux flow model shows, the flux pinning properties of $Tl(Ba_{2-y}Mg_y)Ca_2Cu_3O_{10-\delta}(0.0\leq y\leq 1.5)$ different dc magnetic fields have been used to study materials. The majority diffraction lines in samples are fitted to orthorhombic structure using PMMM space group, according to X-ray diffraction scans of these samples. When the concentration of doping exceeds y=1.0, impurity peaks start to emerge from the background;

samples with y = 1.5 have sufficient impurity phase concentration. These samples have shown for Mg doping of y = 0, 0.5, 1, and 1.5, zero resistivity critical temperatures at 91.5, 97.3, 98, and 97.1 K, respectively, in zero-field measurements of temperature's effect on electrical resistivity (ρ). These Tc values are lower than the one seen in $Cu_{0.5}Tl_{0.5}Ba_2Ca_2Cu_3O_{10-}\delta$ superconductors. $\rho(H,T) = \rho_0 \exp\left(\frac{-U(H)}{k_B T}\right)$; the Boltzmann constant is denoted by k_B, and the activation energy by U. This formula is known as the Arrhenius law for superconductors. The activation energy of superconductor samples was calculated using the Arrhenius plots. Mg-doped Tl-1223 samples have a higher activation energy than undoped samples under a zero magnetic field, according to the graph between activation energy and magnetic field strength. Compared to y = 0, 1, and 1.5, with y = 0.5 the sample has the highest activation energy in the infield measurements. Magnetic field strength of up to 2.89 kG, all compositions experience a rapid decrease in activation energy value; after that, the rate of decline in activation energy value slows. The final compound's increased population of vortex creation is most likely the cause of the decreasing activation energy more slowly as the external magnetic field increases. It appears that the density of pinning centers has increased in these samples based on the rise in activation energy for the sample with y = 0.5, developing an enhancement in their flux pinning character. The superconducting transition width ΔT of sample when there is an applied dc magnetic field, reveals that the smallest transition width is found in the sample with y = 0.5 at zero field ΔT, on the other hand, it is increasing as the charge reservoir layer's Mg content has increased. The excess conductivity study of this sample reveals that Mg doping suppresses the interlayer coupling J, the phase relaxation time of the carriers τ_ϕ, the Fermi velocity of the carriers v_F, and the coherence length $\xi_C(0)$ along the c-axis. The analysis of excess conductivity & magneto resistivity are consistent. $B_{c0}(T)$, $B_{c1}(T)$, and Jc(0) values has increased due to the Mg-doped samples' improved flux pinning characteristics, but the Mg-doped materials' topmost layer exhibits reduced magnetic field penetration depth.

Ö. Çiçek et al. [14] by using solid-state approach, YBCO superconducting samples with composition of $Y(Ba_{1-x}Mg_x)_2Cu_3O_{7-}\delta$, where x = 0.0, 0.5, 1.0, and 1.5, were synthesized. Up to $\pm$9 T applied fields, structural, electrical transport, and magnetic characterizations were carried out. The Mg15 sample displayed a very high resistance value both at room temperature and at 4.2 K, according to electrical measurement, (T) in the temperature range between 300 and 60K, and under applied magnetic field up to 9 T. By showing electron-phonon scattering is the predominant

mechanism in the Pure, Mg05, and Mg10 samples, the resistivity values of the samples dropped linearly from 300 K to Tc. Due to the disturbance of structural order at the atomic level, scattering increases as Mg content in the matrixes rises. Activation energy of samples is calculated from the Arrhenius plots. As the magnetic field and Mg concentration increased, U(H) values for all samples started to decrease. In this scenario, flux mobility and flux trapping both have a role in the decrease in U(H) with rising Mg concentration. The crystal symmetry was unaffected by the Mg substitution, according to XRD patterns, however the crystal properties changed. MgO and Y-211, two impurity phases that were produced, became the dominating ones at high substitution ratios.

Kareem A. Jassim et al. [15] Studied HTSCS with composition $Tl_{0.6}$ $Pb_{0.4}$ $Ba_{2-x}Sr_xCa_2Cu_3O_9$, have been successfully synthesized by using solid state reaction method. The following values were used as substitutes for this compound: x = 0.0, 0.10, 0.20, 0.30, 0.40, and 0.50. The final calcination occurred at 1073 K, and the sintering temperature ranged between 1128 and 1133 K. The transition temperature Tc is found using electrical resistivity and the four-probe method. The maximum Tc(offset) for $Tl_{0.6}Pb_{0.4}Ba_{1.5}Sr_{0.5}Ca_2Cu_3O_{8.76}$ is 113K. The usage of O_2 flow had been used to prepare each sample. The samples that had been doped with Sr showed a pseudo-tetragonal structure with an increase in the c-axis lattice constant in comparison to the samples that had no Sr content, according to X-ray diffraction (XRD) examination. The impact of concurrent strontium Sr replacement at the Ba site within the oxygen-deficient Ba-O layer of $Tl_{0.6}Pb_{0.4}Ba_{2-x}Sr_xCa_2Cu_3O_9$ (with x = 0.00, 0.10, 0.20, 0.30, 0.40, and 0.50) cuprate superconductor has been studied, according to the authors. The two-step solid state reaction methodology had been applied to organize bulk polycrystalline materials. It was discovered that the samples with different Sr concentrations had undergone gross structural characterization using the X-ray diffraction (XRD) method. Each sample has a pseudo-tetragonal structure with an excessive superconducting Tl (Pb)-1223 ratio segment, according to the XRD data acquired from a number of samples. It has been found that the Tc fluctuates depending on how much strontium is present. It has been found that the composition's premiere Tc(offset) is 113 K

References

[1] K. Konstantinov and S. Karbanov, J. Superconductivity 4 (1991) 45-47.

[2] S. Mazumder, H. Rajagopal, A. Sequeira, Jagriti Singh, A. K. Rajarajan, L. C.

Gupta, and Vijayaraghavan, Phase Transition 19 (1989) 97-105.

[3] Nawazish A. Khan and Shahid Nawaz, IEEE Transactions on Applied Superconductivity 16 (2006) 2-8.

[4] Nawazish A. Khan, M. Shamraiz, S. Abbas and Azhar A. Rizvi, J Supercond Nov Magn 27, 2005 (2014).

[5] N.A. Khan, A.A. Khurram, Appl. Phys. Lett. 86 (2005) 1–3.

[6] N.A. Khan, G. Husnain, Phys. C Supercond. Its Appl. 436 (2006) 51–58

[7] Agarwal, S., et al., Superconductivity in the Mg-doped $CuBa_2Ca_3Cu_4O_{12-y}$ system. Physical Review B, 1998. 58(14): p. 9504.

[8] Kashif Naseem, Nawazish A. Khan, and Syed Hamza Safeer, Journal of ELECTRONIC MATERIALS, Vol. 50, No. 4, 2021.

[9] Nawazish A. Khan ∗, Najmul Hassan, Journal of Alloys and Compounds 464 (2008) 550–555

[10] R Awad et al R. Awad[1] , I. H. Ibrahim[1,2] , E. M. E. Mansour[3] , M. Roumie[4] and A. Zein[2] 2008 J. Phys.: Conf. Ser. 97 012323

[11] Palstra, T.M., Batlogg, B., Schneemeyer, L.F., Waszczak, J.V.: phys. rev. Lett 61, 1662(1988)

[12] H. Abbasi ∗, J. Taghipour, H. Sedgh, Journal of Alloys and Compounds 482 (2009) 552–555

[13] Shakil Ahmad · Nawazish A. Khan · A. A. Khurram · Sajjad Hussain J Supercond Nov Magn (2014) 27:2787–2794

[14] Ö. Çiçek∗ and K. Yakinci ACTA PHYSICA POLONICA A Vol. 142 (2022)

[15] Jassim, K.A. and T.J. Alwan, The effect of simultaneous substitution of strontium at the barium site of $Tl_{0.6}Pb_{0.4}Ba_{2-x}Sr_xCa_2Cu_3O_{9-\delta}$ superconductors. Journal of superconductivity and novel magnetism, 2009. **22**(8): p. 861.

Chapter No: 03

Synthesis and Experimental Techniques

3.1 Synthesis Techniques

A solid state thermochemical reaction is the simplest method employed in the current work for the synthesis of ceramic material. Various techniques are used to produce high Tc superconductors. Therefore, a solid state reaction approach was employed to create our samples because it is more efficient and suited for usage than other methods due to performance and reliability.

3.1.1 Solid State Reaction Method

In this method, solid materials are used as reactants to create polycrystalline ceramic superconductors. The structural characteristics, surface area, and reactivity of the reactants all affect reaction rate [1]. To improve the interaction between the reactants, they are first all ground together. Precursors are heated to high temperatures because it takes a significant amount of energy to overcome lattice energy. A high rate of atom mobility is supported at the given temperature. In the lattice, atoms move slowly, but by raising the temperature, they can move quickly [2]. Calcination and sintering are the two main steps in the solid-state reaction process. Solid oxides that undergo calcination are broken down into their corresponding elements, which are then mixed once again to produce a new product. The sintering process enhances the product's grain size and crystal structure.

3.1.2 Synthesis of Samples

Using a solid state reaction technique $(Cu_{0.5}Tl_{0.5})Ba_2(Ca_{2-y}Mg_y)(Cu_{2.5}Cd_{0.5})O_{10-\delta}$ (y=0, 0.25, 0.5). $Cu_2(CN)_2$+H_2O, $Ba(NO_3)_2$, $Cd(NO_3)_2$,$Ca(NO_3)_2$, MgO, and Tl_2O_3 compounds were used as starting materials for the production of these samples. There are two steps in the synthesis process we used. The precursor materials $Cu_{0.5}Ba_2(Ca_{2-y}Mg_y)(Cu_{2.5}Cd_{0.5})O_{10-\delta}$ were produced at the first stage. The previously mentioned substances, with the exception of Tl_2O_3, were combined in the appropriate quantities and ground for an hour to create the precursor. The powder was then placed in quartz boats and heated to 860°C for 24 hours. Afterward, the furnace was cooled to room temperature. The samples were heated under similar conditions for 24 hours in alumina boats to achieve homogeneity after intermediate grinding was completed for an hour. At the second stage, a calculated amount of Tl_2O_3 was added to the precursor and ground for an hour. In a hydraulic

press from Carver, Tl-mixed powders were pelletized under 4 tons/cm^2 of pressure. To prevent the loss of Tl, these pellets were placed in gold capsules and sintered for 10 minutes at 860°C before being quenched to room temperature.

3.2 Characterization Techniques

We can discuss about theoretical and experimental approaches to sample characterization in this part. The following techniques are used to describe the prepared samples.

- X-Ray Diffraction.
- A Resistivity Measurement.

3.2.1 X-Ray Diffraction (XRD)

To learn more about a sample's crystal structure, including lattice characteristics, stress and strain measurements, phase analysis, defects, crystallite size, and the identification of unidentified materials, the XRD technique is used. Only when the wavelength of light shining on the crystal structure is similar to the distance between planes can diffraction occur. As x-rays' wavelength (10 nm) meets that requirement, they are employed to analyze crystal structure. A crystal with x-ray diffracting properties has a natural grating. [3]

3.2.1.1 Bragg' s Law

XRD uses Bragg's law. Lawrence Bragg and Henry Bragg, a father and son team, made the initial proposal. They discovered that crystalline materials can reflect x-rays at specific angles. X-rays are electromagnetic waves with a short wavelength and high energy.

Consider two monochromatic x-rays beams striking a crystal with d interplanar space. Consider it is incident at an angle. The crystal reflects both beams at the same angle. By creating the perpendiculars A_1B and A_1C, one can determine the path difference between the two beams.

Path Difference= BA_2+A_2C

$BA_2=A_2C=d\ Sin\theta$

Path Difference= $d\ Sin\theta$ (3.1)

Only when the path difference between two reflected waves is an integral multiple of their wavelengths can constructive interference take place. The condition for constructive interference is thus:

$$2\,d\sin\theta = n\lambda \qquad (3.2)$$

"n" is a positive integer in this case. If the x-ray wavelength is known, the well-known Bragg's equation (3.2) can be used to calculate d. The basis for x-ray crystallography was established by applying Bragg's law to analyze crystal structure [4].

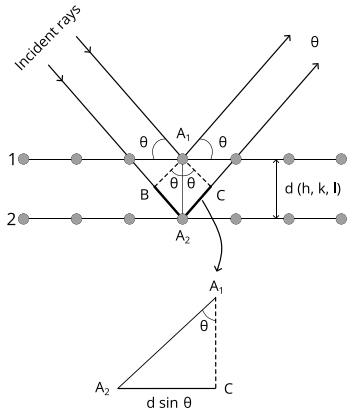

Fig 3.1: Pictorial diagram of Bragg's law

3.2.1.2 X-Ray Diffractometer

X-rays are incident on material and then interact with it, producing a scattering pattern that helps in the identification of crystal structure in an x-ray diffractometer. An x-ray diffractometer is made up of the following parts.**:**

- X-Ray Source
- Sample holder
- X-Ray Detector

X-rays are produced by cathodes and are then filtered to create monochromatic radiation. The majority of target materials used to generate x-rays with wavelengths of 0.8A^o and 1.54A^o, respectively, are Mo and Cu [5]. When the sample is collimated and x-rays are shined, the phenomenon of diffraction takes place. The intensity of the reflected x-ray beams is measured by the counter as the sample holder and x-ray detector rotate constantly. The sample, counter, and x-ray source are all on the same plane. The counter's angular displacement is given by 2θ and it

rotates around its axis. In order to achieve a similar angle of incidence and reflection, the sample and counter are arranged so that if a sample is moved by an angle, the counter will move by an additional angle. The strength of the diffracted rays is measured as a function of 2θ.

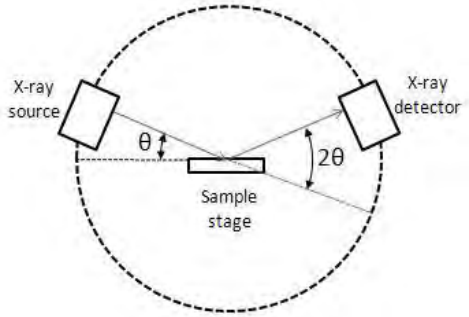

Fig 3.2: X-ray Diffractometer

Sample Analysis:

- The crystal's reflected x-ray photons are counted by the detector and shown on a computer screen as a pattern thanks to a computer system. Identifying the crystal structure is made possible by comparing this pattern to a reference pattern. The lattice parameters are discovered using the Checkcell program.
- The crystalline or amorphous nature of the crystal structure is determined through X-ray diffraction examination. The structure is crystalline if there are more distinct intensity peaks than amorphous ones. [6]
- To determine the grain size of polycrystalline material, use the whole width at half maximum rule. This rule's mathematical formulation is as follows:

$$\tau = \frac{0{\cdot}9\lambda}{\beta \cos\theta_B} \qquad (3.3)$$

where grain size, Bragg's angle, and full width at half maximum

and λ is the x-ray wavelength. The complete width at its maximum can be written as follows:

$$\beta = \frac{1}{2(2\theta_1 - 2\theta_2)} \qquad (3.4)$$

The unit cell's density is determined by:

$$\rho = \frac{\sum A/N_A}{V} \qquad (3.5)$$

N_A Avogadro's number, V Volume of a unit cell, and ΣA Sum of All Atomic Weights.

3.2.1.3 Methods used for x-ray diffraction

- **Laue's method**

This technique uses x-rays to target stationary crystal at a fixed incident angle θ. Only the wavelength of incident rays varies. Only crystal planes whose geometry agrees to Bragg's law will allow these various wavelength beams to reflect.

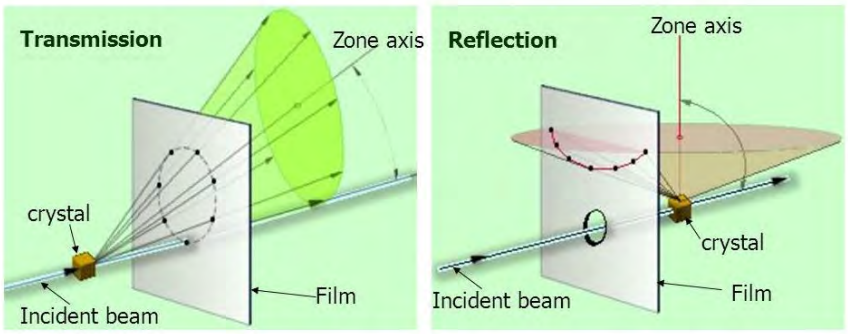

Fig 3.3: Laue's Transmission Method

- **Rotating Crystal method**

This technique involves placing the crystal first normal to the x-ray beam and then in a thin cylindrical film. The crystal starts to revolve along its axis when the X-ray beam sparkles on it. While angle of incidence "θ" changes in this situation, the x-ray wavelength "λ" remains constant. Despite the fact that x-rays are shone at several sets of planes, only those planes that create the proper Bragg angle with incident x-rays will experience diffraction.

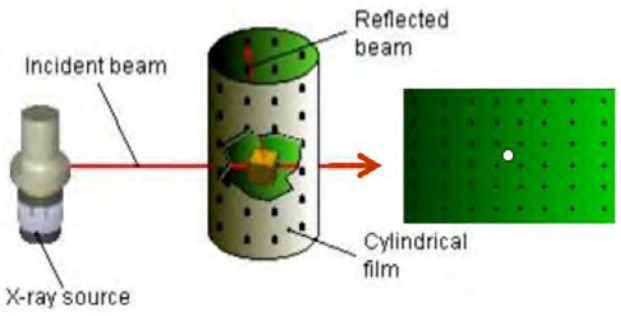

Fig 3.4: Determining the crystal structure by rotating sample

3.2.2 Resistivity Measurements

As the conductor has free electrons, they can travel in any direction without restriction. But, when a voltage is applied, all of the electrons move in the same direction and create a current that flows through the conductor. The resistance (R) in a conductor, which can be computed using Ohm's equation, is caused by the lattice/phonon and imperfections in the conductor that hinder electron transport.

$$V = IR$$

Here, "I" indicates the current that is going through the conductor. "V" denotes the voltage applied across the conductor's ends, and "R" denotes the resistance of the conductor. A conductor's resistance is inversely related to its cross-sectional area (A) and directly related to its length (L).

$$R = \frac{\rho L}{A} \qquad (3.6)$$

The term "ρ" used here refers to the conductor's resistivity, which is a function of temperature.

$$R(T) = \rho_{(T)} \frac{L}{A}$$

$$\rho_{(T)} = R_{(T)} \frac{A}{L} \qquad (3.7)$$

The Ohm's law, however,

$$R_{(T)} = \frac{V}{I}$$

$$\rho_{(T)} = \frac{VA}{IL} \qquad (3.8)$$

Here, we measure length in cm, area in cm^2, current in amperes, and voltage in volts so that the resistivity is measured in the form of Ω-cm.

3.2.2.1 Four Probe Resistivity Method for Resistivity Measurements

With two-probe resistivity, resistivity may be measured up to m. Nonetheless, we can use the four-probe method to measure resistivity up to m-m or micro-ohm-meter. This approach is typically used to compute the resistivity of metals, polymers, semiconductors, and superconductors. Figure 3.5 depicts the experimental setup for the Four Probe Resistivity Measurement technique. Using this technique, four contacts are adhered with silver paste on the sample's surface in such a way that when the sample is chilled to an incredibly low temperature, they won't shatter. The outside wires maintain the current flow while the inner wires display a drop in voltage across the sample. The resistance of the sample is the reason for this voltage decrease that is being reported. We opted for the four-probe strategy instead of the two-probe method since the contact resistance significantly affects the sample's overall resistance. As a result, we only use the four probe technique to measure the resistance across the sample; the contact resistance is left out.[7]

If "V" is voltage drop across sample and "A" is cross-sectional area through which current "I"

flows through the sample, then the resistivity of the sample is defined as follows.

$$\rho_{(T)} = \frac{VA}{IL}$$

As a result, V(T) is a temperature-dependent variable and L is the distance between the inner voltage wires.

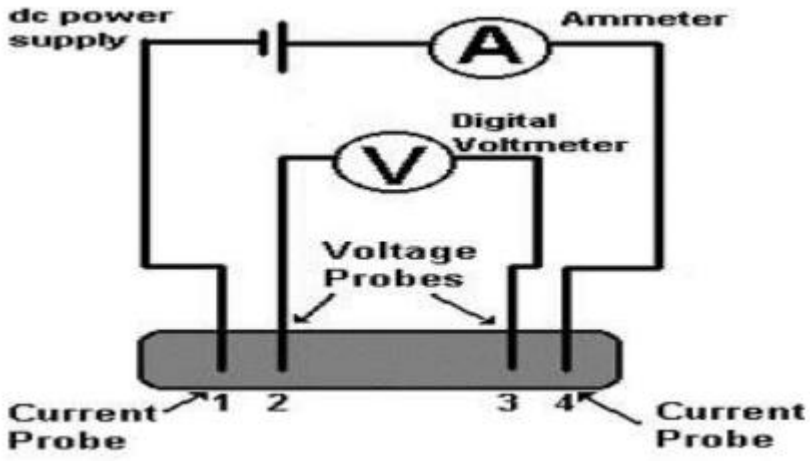

Fig 3.5: Schematic Diagram of Four-point probe

3.2.2.2 Physical Property measurement System

A unique idea in laboratory equipment is the Quantum Design PPMS, an open architecture, variable temperature-field system with several automated measuring functions. Measurement options contain the necessary electronics and hardware to start collecting publication-quality data right away, and the system is easily adapted to custom user experimentation. Temperature ranges of 2K - 400 K and the fields up to ±9 T are examples of sample environment controls. The PPMS is the most flexible system of its type because of its versatile design, which allows for the combination of numerous features into a single device.

Fig 3.6: Physical measurement system

Features:

- In accordance with more than 20 Quantum Design Measurement Options, which easily integrate with the MultiVu software environment.
- For consistently reliable electrical access, adaptable sample mounts couple readily to the 12 electrical leads integrated within the cryostat insert.
- Complex data acquisition techniques can be easily automated using software controls for magnetic field and temperature.
- Basic system functioning no longer requires the usage of or purchase of external bridges, current sources, or voltage sources due to the integrated Model 6000, a powerful microprocessor-controlled device.
- The diameter of the sample chamber is 2.6 cm for handling custom probes.
- Connectivity to external third-party instruments, whether via MultiVu itself or via other software like NI LabVIEW, for the purpose of commanding the PPMS.

DC Resistance:

DC resistance on up to three channels using a standard puck can be measured using the DC Resistivity Option**.**

- Measure resistances of 10 μΩ to 5 MΩ in the standard 4-probe configuration.
- Source currents between 2 nA to 8 mA.
- Configurable bridge parameters to limit the voltage, current, or power at the sample for protecting the sensitive devices, films, etc.

3.2.2.3 Magneto-resistivity Measurements

The change in a material's resistivity when a magnetic field is present is known as magnetoresistance. William Thomson made this discovery in 1851. The reason for this effect is because in the presence of a magnetic field, electron trajectories are altered and no longer precisely follow the electrical field's orientation that is superimposed. The strength of the magnetic field and the angle between it and the direction of the current have a role in the magnetoresistance effect.

There are often four categories used to characterize magnetoresistance.

1) Ordinary magnetoresistance
2) Giant magnetoresistance
3) Anisotropic magnetoresistance
4) Colossal magnetoresistance

- **Ordinary Magnetoresistance**

At low fields, non-magnetic metals have a small magnetoresistance impact. For high fields, the effect can, however, get extremely considerable. Magnetic fields that are parallel and perpendicular to the direction of the current cause a positive change in resistivity $\Delta\rho$, however $\rho_{\perp}$is typically greater than ρ_{II}. There are three types of ordinary magnetoresistance, depending on how the electron orbitals are arranged at the fermi surface.

I. The orbits of the electrons in K space are constrained. in metals with closed fermi surfaces, and the magnetic field raises the electron's closed orbital cyclotron frequency. In this situation, extremely strong magnetic fields cause the resistance to saturate.
II. **H** has a direct effect on magnetoresistance and is unaffected by the crystallographic direction for metals with an equal amount of holes and electrons.
III. Fermi surfaces in metals that have open orbits in some crystallographic orientations will exhibit high magneto resistance when magnetic fields are applied in those directions. While in other directions, where the orbits are closed, the resistance will saturate.

- **Giant Magnetoresistance**

The first case of this form of resistance was found in anti-ferromagnetically linked layers of Fe/Cr in 1988. Thin magnetic layers are separated from others in this structure by layers of non-magnetic metals. Depending on the thickness of the non-magnetic layers, the magnetic layers were either ferromagnetically or antiferromagnetically linked to them.

- **Anisotropic Magnetoresistance**

MR effect in ferromagnetic metals and alloys indicates that values of $\frac{\Delta\rho}{\rho}$ in the range of 2% are attained in weak magnetic fields. $\Delta\rho_{\parallel}$ in this situation grows as the magnetic field gets stronger, whereas $\Delta\rho_{\perp}$ drops as the magnetic field becomes greater. Spin orbit coupling is the basis for magnetoresistance. The rotation of the magnetization causes a small deformation of the electron cloud surrounding each nucleus. The amount of scattering that conduction electrons undergo as they go through the lattice is altered by this deformation.

- **Colossal Magnetoresistance**

Materials with pervoskite structures can exhibit this type of magnetoresistance such as

$La_{1-x}M_xMnO_{3+}\delta$ (M= Sr, Ca). The term "colossal" originated from didactic effects on order of $\frac{\Delta\rho}{\rho}$=125000% that were seen. A material's resistivity changes to a change in behavior from insulating to metallic at low temperatures. In metallic regime, the CMR impact is significant.

3.2.2.4 Magnetoresistance Measurement Setup

The following describes our magneto resistance setup:

- Four Probe resistivity arrangements
- Electromagnetic from Mitsubishi steel magnetic co Ltd, of maximum field 1.3T
- Constant current power supply from chyo Balance Kyoto, Japan corporation
- Digital Gauss meter, DGM-102

At various magnetic fields, we investigated the magnetoresistance of our superconductor samples. The range of the magnetic produced is 0 to 12.8 kG. In the temperature range around the superconducting transition, the samples' magnetoresistance has been determined.

3.3 Computational Analysis

3.3.1 Arrhenius Plot

The Arrhenius plot of superconductors under various dc magnetic field was done. For this plot, take the logarithm of resistivity and inverse the temperature. Then plot the $\log(\rho)$ on y-axis and temperature inverse (T^{-1}) on x-axis. This gives the Arrhenius plot of superconductors.

3.3.2 Activation Energy of Superconductor

Activation energy of superconductors is calculated from the Arrhenius plots. For calculation of activation energy, find the slope of Arrhenius plots, then multiply the slope with the Boltzmann constant k_B.This gives the activation energy of superconductors. After this, graph is plotted between activation energy and various magnetic fields.

3.3.3 Fluctuation Induced Conductivity Analysis (FIC)

The method of studying fluctuations in superconductors caused by the formation and destruction of Cooper pairs down to onset temperature is known as "fluctuation induced conductivity analysis," also known as "para conductivity analysis." Above the transition temperature, cooper pairs begin to form, but due to thermal fluctuation, these pairs keep forming and dissipate until Tc(R=0). Fluctuations in the superconductor are caused by the creation and destruction there. The density of fluctuation drops as we cool our sample below Tc(R=0), where thermodynamic fluctuation is unable to effectively interact with the creation of cooper pairs. Condensation of cooper pairs consequently occurred, resulting in negligible resistance [8]. For a temperature range approaching Tc known as the Ginzburg criterion temperature, these fluctuations that produce conductivity exhibit (TG). The value of TG for HTSCs is between 1-2 K, but it is less than 1μK for low temperature superconductors. As a result, these fluctuations can be analyzed. Ginzburg was the first scientist to investigate how fluctuations affect heat capacity and to calculate the value of temperature at which these changes are significant, as shown by the relation below;

$$\frac{\Delta T}{T_c} \sim \left[\frac{(\Delta T)^4}{\varepsilon_f}\right] \sim \left[\frac{(a)^4}{\xi}\right] \sim 10^{-4} to\ 10^{-16} \qquad (3.10)$$

Here, "a" stands for the interatomic distance between two lattice sites, and "ξ" stands for the coherence length.

3.3.3.1 Aslamazov-Larkin Theory

The fluctuations in Ψ(r) of HTSC are mostly caused by short coherence lengths and high Tc. These variations can be found in laboratories using fluctuating conductivity, fluctuating magnetoconductivity, and fluctuating specific heat. The first theoretical approximations for fluctuation induced conductivity (FIC), which are used to assess the resistivity measurements of a sample, were developed by Aslamazov and Larkin. Aslamazov and Larkin developed the FIC of crystallites based on the Ginzburg-Landau theory in 1968 [9]. They claim that the FIC is characterized by "$\Delta\sigma_{2D}$" and "$\Delta\sigma_{3D}$" in the two- and three-dimensional regimes, respectively.

$$\Delta\sigma_{2D} = \frac{e^2}{16\hbar d}\left(\frac{T}{T-T_c}\right) \tag{3.11}$$

$$\Delta\sigma_{3D} = \frac{e^2}{32\hbar\xi_0}\left(\frac{T}{T-T_c}\right)^{1/2} \tag{3.12}$$

Using A.K. Ghosh et al. [10], the FIC analysis of the polycrystalline samples is suggested. Actually, the AL equations were altered as

$$\Delta\sigma_{2D} = \frac{e^2}{64\hbar d}\varepsilon^{-1}[1 + (1 + \frac{8\xi^4(0)\varepsilon^{-1}}{d^2\xi_{ab}^2(0)})^{1/2}] \tag{3.13}$$

$$\Delta\sigma_{3D} = \frac{e^2}{32\hbar\xi_p(0)}\varepsilon^{-\frac{1}{2}} \tag{3.14}$$

where "$\xi_P(0)$" stands for the response of polycrystalline materials, or effective coherence length, and "ε" stands for the reduce temperature. $\xi_P(0)$ is presented as

$$\frac{1}{\xi_P(0)} = \frac{1}{\xi_c(0)} + (\frac{1}{\xi_c^2(0)} + \frac{1}{\xi_{ab}^2(0)})^{1/2} / 4 \tag{3.15}$$

The intersection of the critical regime and the 3D regime produces the Ginzburg number NG and temperature TG in the transition region. The TG is the temperature at which the 3D LD regime and the Ginzburg Landau (GL) regime cross over. The essential superconducting parameters are

derived using the Ginzburg-Landau theory, the TG and NG expression, and the following relationships.

$$N_G = \left|\frac{T_G - T_c^{mf}}{T_c^{mf}}\right| \qquad (3.16)$$

$$NG = 1/2[KBTc/Bc(0)2\gamma 2\xi c(0)3]2$$

The values of the NG are determined from this equation to be 0.045, 0.048, and 0.045, respectively.

References

[1] M. Paulus and P. Hagen Muller, Preparative methods in Solid State Chemistry, Academic Press, New York, 487 (1972).

[2] I. Parkin, Chemical Society Reviews 25(3), 199 (1996).

[3] J.S. Blakemore, Solid State Physics, Cambridge University Press, (1985).

[4] W.H. Bragg and W.L. Bragg, Proc. R. Soc. Lond. A 88, 428 (1913).

[5] B.E. Warren, X-ray Diffraction, Dover Publications, (1969).

[6] J.S. Blakemore, Solid State Physics, Cambridge University Press, (1985).

[7] N.W.A. and N.D. Mermin, Solid State Physics, World Publishing Corporation, (1976).

[8] M.A.R. · S.A. · N.H. · N.A.K. Khan, J Supercond Nov Magn 27.11 (2014) 2427–2434.

[9] Aslamasov, L. and A. Larkin, The influence of fluctuation pairing of electrons on the conductivity of normal metal. Physics Letters A, 1968. **26**(6): p. 238-239.

[10] Ghosh, A., S. Bandyopadhyay, and A. Basu, Generalization of fluctuation induced conductivity in polycrystalline Y 1− x Ca x Ba 2 Cu 3 O y and Bi 2 Sr 2 Ca 1 Cu 2 O 8+ δ superconductors. Journal of applied physics, 1999. **86**(6): p. 3247-3252.

Chapter No: 04

Results And Discussion

4.1 Introduction:

Simple crystal chemistry of (Cu-Tl)-based high temperature superconductors (HTSCs) shows that they are endowed with a charge reservoir layer supplying free carriers to superconducting planes. Intrinsic reason for providing carriers to the conducting planes through the charge reservoir layer is their higher Fermi-level in comparison with the CuO_2 conducting planes. The copper atoms in the CuO_2 planes possess a small spin owing to their $3d^9$ state. The under reason for the higher critical temperature in such oxide superconductors is existence of this small spin that brings phase coherence of the carriers in various planes. Therefore, Ca^{+2} atoms separating the CuO_2 planes play a vital role in determining such phase coherence of carriers in various CuO_2 planes. These atoms determine equilibrium distance at which CuTl-1223 system attains its energy minimum and hence an inter-plane coupling. We can artificially decrease the separation between the various CuO_2 planes by doping relatively smaller sized atoms, in comparison with Ca atoms and hence can increase the inter-plane coupling. Because of increased inter-plane coupling the interactions of small spins for Cu ($3d^9$) atoms increase that in turn would increase the phase coherence of carriers in various planes. Such experiments would help in understanding the reason why oxides have high Tc superconducting. We doped Mg^{+2} at Ca^{+2} sites for these investigations in $(Cu_{0.5}Tl_{0.5})Ba_2\left(Ca_{2-y}Mg_y\right)(Cu_{2.5}Cd_{0.5})O_{10-\delta}$ superconductors $y = (0, 0.25, 0.5)$ samples; The atomic radius of magnesium (1.6A^o) is smaller as compared to Ca(1.97A^o). Moreover, the electronegativity of Mg (1.3 pauling) is higher than Ca(1.0 paulings).

4.2 Experimental:

By the two steps solid-state reaction method $(Cu_{0.5}Tl_{0.5})Ba_2\left(Ca_{2-y}Mg_y\right)(Cu_{2.5}Cd_{0.5})O_{10-\delta}$superconductors (y=0, 0.25, 0.5) samples were prepared in two stages. In first step, the compounds such as$Ca(NO_3)_2$, $Ba(NO_3)_2$, $Cd(NO_3)_2$, $MgO$and $Cu_2(CN)_2 \cdot H_2O$ were ground in a calculated quantity in a mortar and pestle for about 1 hour to give $(Cu_{0.5})Ba_2\left(Ca_{2-y}Mg_y\right)(Cu_{2.5}Cd_{0.5})O_{10-\delta}$ superconductors $y = (0, 0.25, 0.5)$ as reactants composition. The ground material was fired twice at 860^{o}C in a pre-heated chamber

furnace in quartz boats for 24 hours and the furnace after the heat treatment was cooled to room temperature. In second step, calculated amount of Tl_2O_3 was added in fired precursor and mixed for sixty minutes to get $(Cu_{0.5}Tl_{0.5})Ba_2(Ca_{2-y}Mg_y)(C_{u_{2.5}}Cd_{0\cdot5})O_{10-\delta}$ superconductors $y = (0, 0.25, 0.5)$ samples as the final reactants compositions. Thallium mixed precursor was then palletized under 4 tons/cm^2 pressure and pellets were enclosed in a gold capsule and heat-treated at 860 ºC in a chamber furnace for 10 minutes. Prepared samples were characterized using X-ray diffraction, temperature-dependent resistance measurements. Phase structures of the samples were calculated using an X-ray diffraction scan by using CuKα radiations of wavelength 1.54056Å and cell parameters were determined by a Checkcell computer program. The sample's Temperature-dependent resistance was determined using the Four-probe method. The magneto resistance measurements of $(Cu_{0.5}Tl_{0.5})Ba_2(Ca_{2-y}Mg_y)(Cu_{2\cdot5}Cd_{0.5})O_{10-\delta}$ superconductors $y = (0, 0.25, 0.5)$ samples are measured in quantum design magnetometer from 0-3T in the temperature regime from room temperature down to 40K.

4.3 Results and Discussions:

4.3.1 XRD analysis

X-ray diffraction scans of $(Cu_{0.5}Tl_{0.5})Ba_2(Ca_{2-y}Mg_y)(Cu_{2\cdot5}Cd_{0.5})O_{10-\delta}$ $y = (0, 0.25, 0.5)$ samples have shown orthorhombic crystal structure in which the c-axis length suppresses and volume of the unit cell increases with increased Mg-doping in the final compound as shown in Figure.

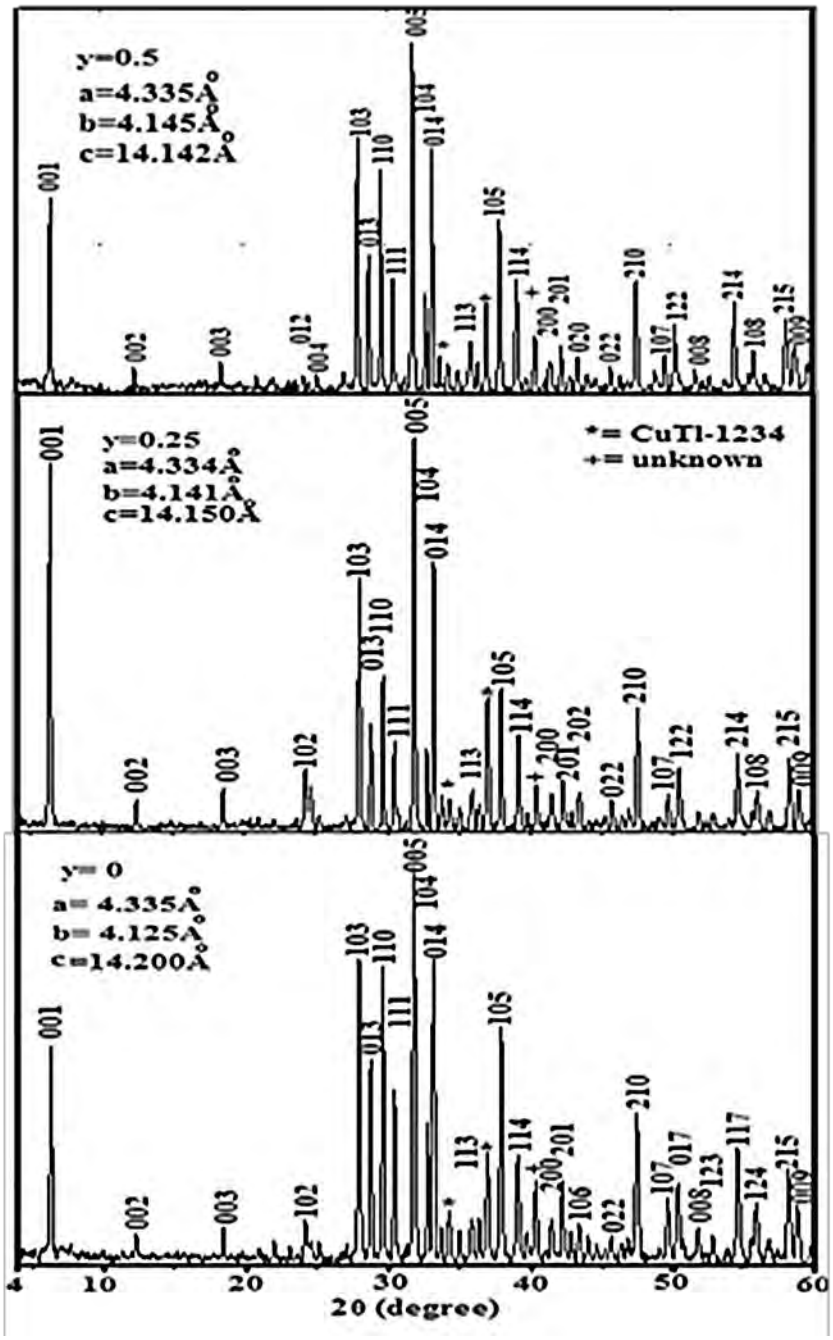

Fig 4.1: X-Ray Diffraction Pattern of $(Cu_{0.5}Tl_{0.5})Ba_2(Ca_{2-y}Mg_y)(Cu_{2\cdot5}Cd_{0.5})O_{10-\delta}$ $y = (0, 0.25, 0.5)$

Sample	a-axis (A°)	b-axis (A°)	c-axis (A°)	Volume
Mg=0	**4.335**	**4.125**	**14.200**	**253.92**
Mg=0.25	**4.334**	**4.141**	**14.150**	**253.95**
Mg=0.5	**4.335**	**4.145**	**14.142**	**254.11**

4.3.2 Magneto Resistivity Measurements

Magneto resistance measurements of $(Cu_{0.5}Tl_{0.5})Ba_2(Ca_{2-y}Mg_y)(Cu_{2\cdot5}Cd_{0.5})O_{10-\delta}$ $y = (0, 0.25, 0.5)$ samples are shown in below figure. The applied external field broadens the transition width and shifts the zero resistivity critical temperatures to lower temperatures with varying degrees in all samples. There are three possible reasons for the broadening of the transition temperature width (1) breaking down of the Cooper-pairs under the influence of applied external force of magnetic field (2) penetration of magnetic field at the inter-granular regions weakly coupled grains (3) penetration of magnetic field within intra-granular regions that in turn generates the vortices there. The increase strength of magnetic field and temperature cycling set these vortices into motion resulting into generation of heat at intra-grain sites. As the motion of vortices is thermally assisted phenomena, therefore, it follows Arrhenius law governed by various activation of energies process. The activation energies of these processes can be calculated following Arrhenius law of the form $\rho\ (T)= \rho_o exp(-U/k_BT)$. In this expression ρ_o is residual resistivity at zero K, U is energy of activation for thermal activated processes and K_B is Boltzmann constant. Since the phase transition do takes place around the transition temperature, therefore, we have used this region for the calculation of activation energy of thermally activated processes.

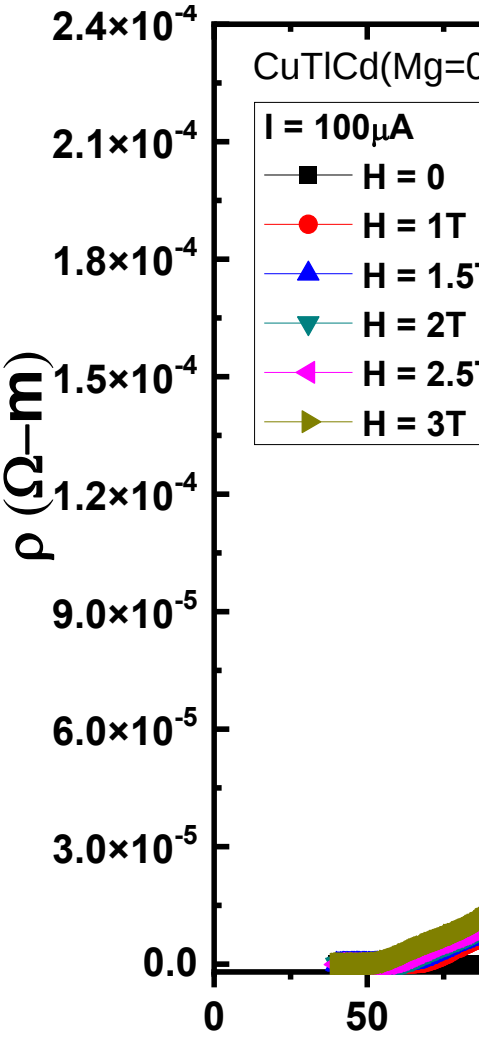
CuTlCd(Mg=0
I = 100μA
H = 0
H = 1T
H = 1.5
H = 2T
H = 2.5
H = 3T
ρ (Ω–m)
2.4×10-4
2.1×10-4
1.8×10-4
1.5×10-4
1.2×10-4
9.0×10-5
6.0×10-5
3.0×10-5
0.0
0
50

(a)

(b)

(c)

Fig 4.2: Resistivity versus Temperature of $(Cu_{0.5}Tl_{0.5})Ba_2(Ca_{2-y}Mg_y)(Cu_{2.5}Cd_{0.5})O_{10-\delta}$ Superconductor under various magnetic fields (a) y=0; (b) y=0.25; (c) y=0.5

Fig 4.3: Resistivity versus temperature plots at zero magnetic field

4.3.3 Arrhenius Plots

The Arrhenius plot of $(Cu_{0.5}Tl_{0.5})Ba_2(Ca_{2-y}Mg_y)(Cu_{2\cdot5}Cd_{0.5})O_{10-\delta}$ $y = (0, 0.25, 0.5)$ samples are shown in fig 4.4(a,b,c). In these plots experimental data points are fitted to the power law of the form $U \sim B^{-\beta}$ and the values of β are in the range of (-0.5 to -0.55) for such samples.

(a)

(b)

(c)

Fig 4.4: The Arrhenius plot of $(Cu_{0.5}Tl_{0.5})Ba_2(Ca_{2-y}Mg_y)(Cu_{2\cdot5}Cd_{0.5})O_{10-\delta}$ $y = (0, 0.25, 0.5)$ under various magnetic fields (a) y=0; (b) y=0.25; (c) y=0.5

Log(ρ) versus 1/T for $(Cu_{0.5}Tl_{0.5})Ba_2(Ca_{2-y}Mg_y)(Cu_{2\cdot5}Cd_{0.5})O_{10-\delta}$ $y = (0, 0.25, 0.5)$ samples in zero applied field are shown in Fig. 4.5.

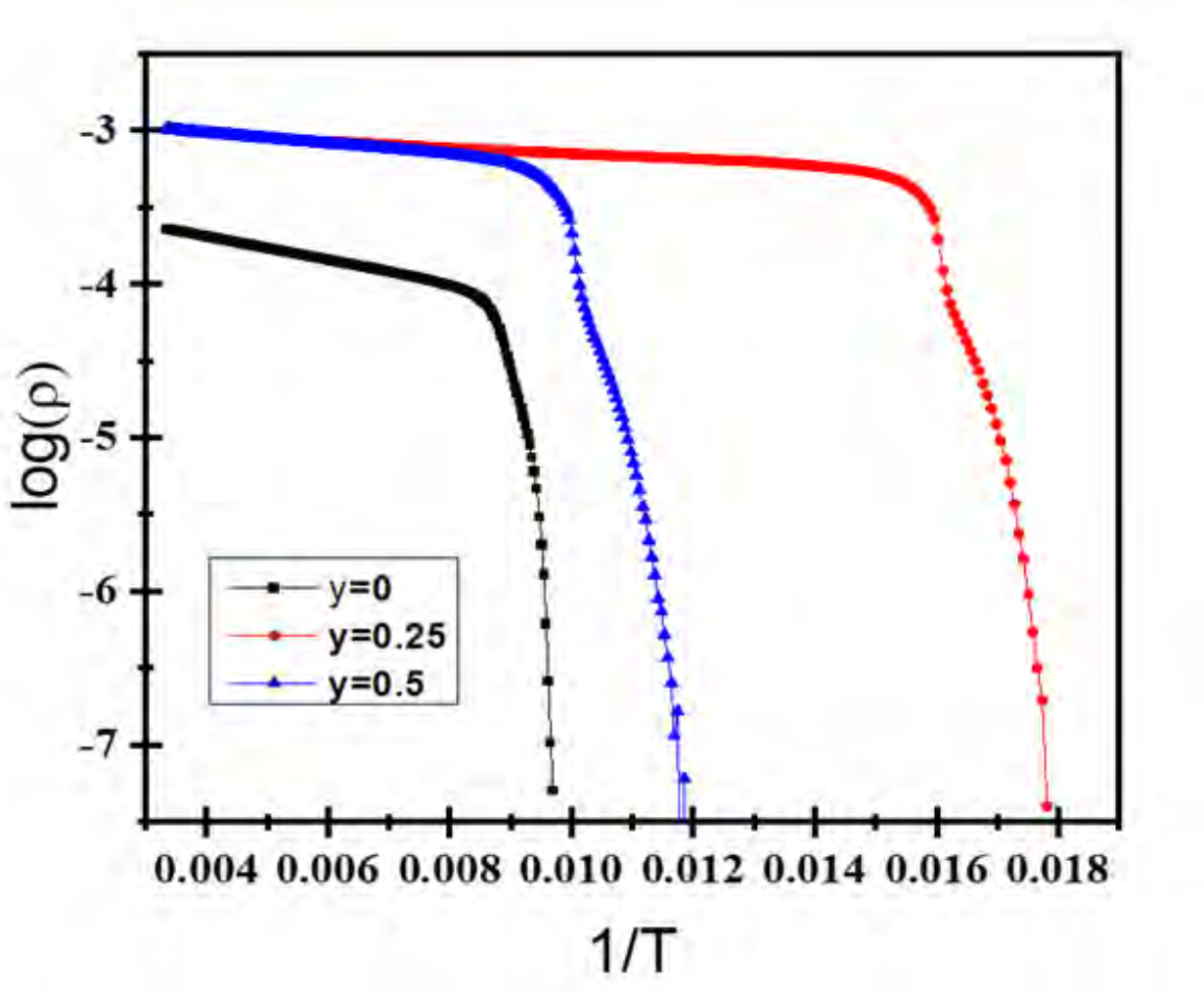

Fig 4.5: Arrhenius plot at zero magnetic field

4.3.4 Superconducting Activation Energy

The activation energy under various fields in all such samples is lower than its value in the absence of magnetic field is manifestation of the fact that application of higher strength magnetic field promotes breaking down of the Cooper-pairs that suppresses their density under higher field. Moreover, the motion of vortices is set in under the applied field resulting into dissipation of heat energy that drives the material in the neighborhood of vortex motion normal. As a result the superconductivity transition temperature is shifted to lower values under higher applied fields and superconducting electrons are weakly coupled. The activation energy for all compositions

$(Cu_{0.5}Tl_{0.5})Ba_2(Ca_{2-y}Mg_y)(Cu_{2\cdot5}Cd_{0.5})O_{10-\delta}$ $y = (0, 0.25, 0.5)$ samples decreases rapidly with the increase strength of applied field. The activation energy of Mg-doped samples is lower in comparison with un-doped samples. This most likely owes to the weaker coupling of the superconducting electrons. It is most likely that shape of the Fermi-surface in doped samples unfold into such a shape that promotes weaker electron-electron coupling. The better inter-plane coupling in Mg-doped $(Cu_{0.5}Tl_{0.5})Ba_2(Ca_{2-y}Mg_y)(Cu_{2\cdot5}Cd_{0.5})O_{10-\delta}$ $y = (0, 0.25, 0.5)$ samples, therefore, promotes weaker-coupling of electrons. It is expected that weakly coupled electrons have longer coherence length. The activation energy in Mg-doped samples suppresses with increased Mg-doping showing weaker coupling of superconducting electrons in the two dimensional Fermi-surface. Moreover, the decrease in the activation energy in doped samples show that their flux pinning characteristics have suppressed and resulted in weaker superconductivity due to decrease distance among CuO_2/CdO_2 planes, hence enhanced an-harmonic oscillations and suppress the superconductivity volume fraction. The activation energy of $(Cu_{0.5}Tl_{0.5})Ba_2(Ca_{2-y}Mg_y)(Cu_{2\cdot5}Cd_{0.5})O_{10-\delta}$ $y = (0, 0.25, 0.5)$ samples as a function of applied magnetic filed shown in figure given below.

Fig 4.6: The Variation of the Activation energy U with the applied magnetic field for $(\boldsymbol{Cu_{0.5}Tl_{0.5}})\boldsymbol{Ba_2}\boldsymbol{(Ca_{2-y}Mg_y)}(\boldsymbol{Cu_{2\cdot5}Cd_{0.5}})\boldsymbol{O_{10-\delta}}\ \boldsymbol{y = (0, 0.25, 0.5)}$

4.3.5 Excess Conductivity Analyses

The excess conductivity analyses [1] of $(Cu_{0.5}Tl_{0.5})Ba_2(Ca_{2-y}Mg_y)(Cu_{2\cdot5}Cd_{0.5})O_{10-\delta}\ y = (0, 0.25, 0.5)$ samples is carried out by following equation:

$$\Delta\sigma_{(T)} = \Delta\sigma_{RT}\varepsilon^{-\lambda_D}$$

This equation can be written in the form:

$$ln\Delta\sigma_{(T)} = ln\Delta\sigma_{RT} - \lambda_D ln(\varepsilon) \qquad (4.1)$$

λ_D is dimensional exponent and $\varepsilon = \left(T - T_c^{mf}\right)/T_c^{mf}$ is reduced temperature used in the neighborhood of T_c. The λ_D is dimensional exponent having values 0.3, 0.5, 1.0 and 2.0 belonging to critical, three dimensional (3D), two-dimensional (2D) and zero-dimensional (0D) regimes of conductivities. These conductivities correspond to various thermally activated processes [2−3] in three dimensional (3D), two-dimensional (2D) and zero dimensional (0D), respectively. The above expression for the polycrystalline samples proposed by Lawrence and Doniach (LD) is:

$$\Delta\sigma_{LD} = [e^2/16\hbar d](1 + J\varepsilon^{-1})^{-1/2}\varepsilon^{-1} \qquad (4.2)$$

Where $J = \left[2\xi_{c(0)}/d\right]^2$ is inter-CuO_2-layers couplings, the d (~15Å in present case) is thickness of superconducting layers and the $\xi_{c(0)}$ is coherence length along the c-axis. The crossover temperatures found by using LD model, lead to the calculation of coherence length:

$$\xi_{c(0)} = \frac{d}{2}\left[\frac{T_{3D-2D}}{T_c^{mf}} - 1\right]^{1/2} \qquad (4.3)$$

The phase relaxation time of the Cooper-pair is determined:

$$\tau_\varphi = \pi\hbar/k_B T_{2D-0D} \qquad (4.4)$$

The coupling constant J by using τ_φ:

$$J = \frac{\hbar\tau_\varphi^{-1}}{2\pi k_B T} \qquad (4.5)$$

The Fermi velocity and the energy needed to breakdown Cooper-pairs:

$$v_F = 5\pi k_B T_c \xi_{c(0)}/2K\,\hbar \quad (4.6)$$

$$E_{Break} = \frac{h}{\tau_\varphi(1.6\times10^{-19})}(eV) \quad (4.7)$$

The co-efficient $K \sim 0.12$ is used according to reference [4]. The crossover temperatures T_G, $T_{3D\text{-}2D}$, $T_{2D\text{-}0D}$ computed from the log plot of the excess conductivity vs the reduced temperature resulting from various thermally activated processes. These cross-over temperatures for $(Cu_{0.5}Tl_{0.5})Ba_2(Ca_{2-y}Mg_y)(Cu_{2.5}Cd_{0.5})O_{10-\delta}$ $y = (0, 0.25, 0.5)$ samples are shown in Figure 4.7 (a, b, c) and table 4.1. With the doping of Mg the T_G, $T_{3D\text{-}2D}$, $T_{2D\text{-}0D}$ are shifted to lower temperatures showing decreased distance among various CuO_2/CdO_2 planes enhances the density of an-harmonic oscillations that suppresses the values of these parameters. The population of inadvertent defects determined by α increases in Mg-doped samples that may act as pinning centers. From the intersection of dimensional exponents various cross over temperature are determined i.e. the slope of λ_{cr} lie below T_G, λ_{3D} having a slope above T_G, λ_{2D} reflect value of slope above $T_{3D\text{-}2D}$ and λ_{0D} referred to the slope of value 2. From these cross-over temperature we have determined the parameters such as $\xi_{c(0)}$, the inter-layer coupling J, V_F (the Fermi velocity) of superconducting carriers, τ_φ (carrier's phase relaxation time) and the energy required to bear-apart the Cooper-pairs. These parameters for $(Cu_{0.5}Tl_{0.5})Ba_2(Ca_{2-y}Mg_y)(Cu_{2.5}Cd_{0.5})O_{10-\delta}$ $y = (0, 0.25, 0.5)$ samples are summarized in table 4.2. The values of $\xi_{c(0)}$, V_F and τ_φ are enhanced with the increased Mg doing owing to the increase in the value of Fermi-vector $K_f=(3\pi^2N/V)^{1/2}$ of $(Cu_{0.5}Tl_{0.5})Ba_2(Ca_{2-y}Mg_y)(Cu_{2.5}Cd_{0.5})O_{10-\delta}$ $y = (0, 0.25, 0.5)$ samples. The Ginzburg number abbreviated as N_G is determined from the crossover temperature between Ginzburg Landau (GL) regime and 3D (LD). This crossover temperature is called T_G. By using the T_G and the T_c of a material, the equation for N_G can be written as [5]

$$N_G = \left[\left(T_G - T_c^{mf}\right)/T_c^{mf}\right] \quad (4.8)$$

Using Ginzburg-Landau theory and above expression of N_G different superconducting parameters are calculated by employing the following equation [6–7]

$$N_G = [1/2]\left[k_B T_c / B_{c(0)}^2 \gamma^2 \xi_{c(0)}{}^3\right]^2 \quad (4.9)$$

$$B_{c(0)} = \Phi_0 / 2\left(\sqrt{2}\right)\pi\lambda_{pd}\xi_{ab(0)} \quad (4.10)$$

$$B_{c(1)} = B_c \ln \kappa / \left(\kappa\sqrt{2}\right) \quad (4.11)$$

$$B_{c(2)} = B_c \kappa \sqrt{2} \quad (4.12)$$

$$J_{c(0)} = 4\kappa B_{c1} / 3\left(\sqrt{3}\right)\lambda_{pd} ln(\kappa) \quad (4.13)$$

The γ tell us about the anisotropy of superconductor having expression $\gamma = \xi ab(0)/\xi c(0) = 5/(n-1)$ and for CuTl 1223 samples with $n = 3$ lead to the value $\gamma = 2.5$ while the $\kappa = \lambda/\xi$ is Ginzburg Landau (GL) parameter [8]**.** Here the mean field critical temperature abbreviated as T_c^{mf} is evaluated from the point of inflection of the temperature of derivative of resistivity $(d\rho/dT)$. By employing Ginzburg Landau number N_G the values the parameters such as $B_{c(0)}$, $B_{c(1)}$, $B_{c(2)}$, $J_{c(0)}$ and $\kappa = \lambda/\xi$ are determined by employing equations (4.10) to (4.13) and these values are compared for $(Cu_{0.5}Tl_{0.5})Ba_2\left(Ca_{2-y}Mg_y\right)(Cu_{2.5}Cd_{0.5})O_{10-\delta}$ $y = (0, 0.25, 0.5)$ samples in tables 4.2. The values of $B_{c(0)}$, $B_{c(1)}$, $J_{c(0)}$ are enhanced in Mg-doped samples confirming the fact that increased population of inadvertent defects in the doped samples source of such enhancement. These localized defects act as efficient pinning centers thereby promoting increase in the values of $B_{c(0)}$, $B_{c(1)}$, $J_{c(0)}$ parameters.

Samples	λ_{cr}	λ_{3D}	λ_{2D}	λ_{SW}	$T_{CR-3D}=T_G$ (K)	T_{3D-2D} (K)	T_{2D-SW} (K)	T_{cmf} (K)	T^{*2D-SW} (K)	$\alpha=\rho_n(0K)$ (Ω-cm)
Mg=0	0.29	0.50	1.01	2.0	115.61	115.98	145.72	112.5	176.73	3.90E-5
Mg=0.25	-	0.48	1.16	1.9	101.68	106	106.73	101.63	143.53	4.31E-4
Mg=0.5	-	0.48	1.13	2.1	100	108.92	109.29	100.11	149.82	5.12E-4

Table 4.1: Parameters calculated from diagram of $\ln(\Delta\sigma)$ vs $\ln(\varepsilon)$

Samples	$\xi_c(0)$ (Å)	J	N_G	$\lambda_{p.d}$ (Å)	Bc (0) (T)	B_{c1} (T)	B_{c2} (T)	K	Jc(0) $*10^3$ (A/cm^2)	V_F*10^6 (m/s)	E_{Break} (eV)	$\tau\varphi$ $*\ 10^{-13}$
Mg=0	0.88	0.03	0.035	196	4.40	1.07	129	12.26	20.59	7.8	0.08	.51
Mg=0.25	1.04	0.04	0.049	98.83	8.74	3.07	129	6.18	81.07	7.9	0.03	1.4
Mg=0.5	1.5	0.01	0.032	59.77	12.93	6.08	129	3.74	221.6	8.1	0.01	3.9

Table 4.2: Parameters calculated from excess conductivity analyses of $(Cu_{0.5}Tl_{0.5})Ba_2(Ca_{2-y}Mg_y)(Cu_{2.5}Cd_{0.5})O_{10-\delta}$ y=0, 0.25, 0.5

Fig 4.7a: $\ln(\Delta\sigma)$ Vs $\ln(\varepsilon)$ depiction of a $(C_{u_{0.5}}Tl_{0.5})Ba_2Ca_2(Cu_{2.5}Cd_{0.5})O_{10-\delta}$

Fig 4.7b: $\ln(\Delta\sigma)$ Vs $\ln(\varepsilon)$ depiction of a$(Cu_{0.5}Tl_{0.5})Ba_2(Ca_{1.75}Mg_{0.25})(Cu_{2\cdot5}Cd_{0.5})O_{10-\delta}$

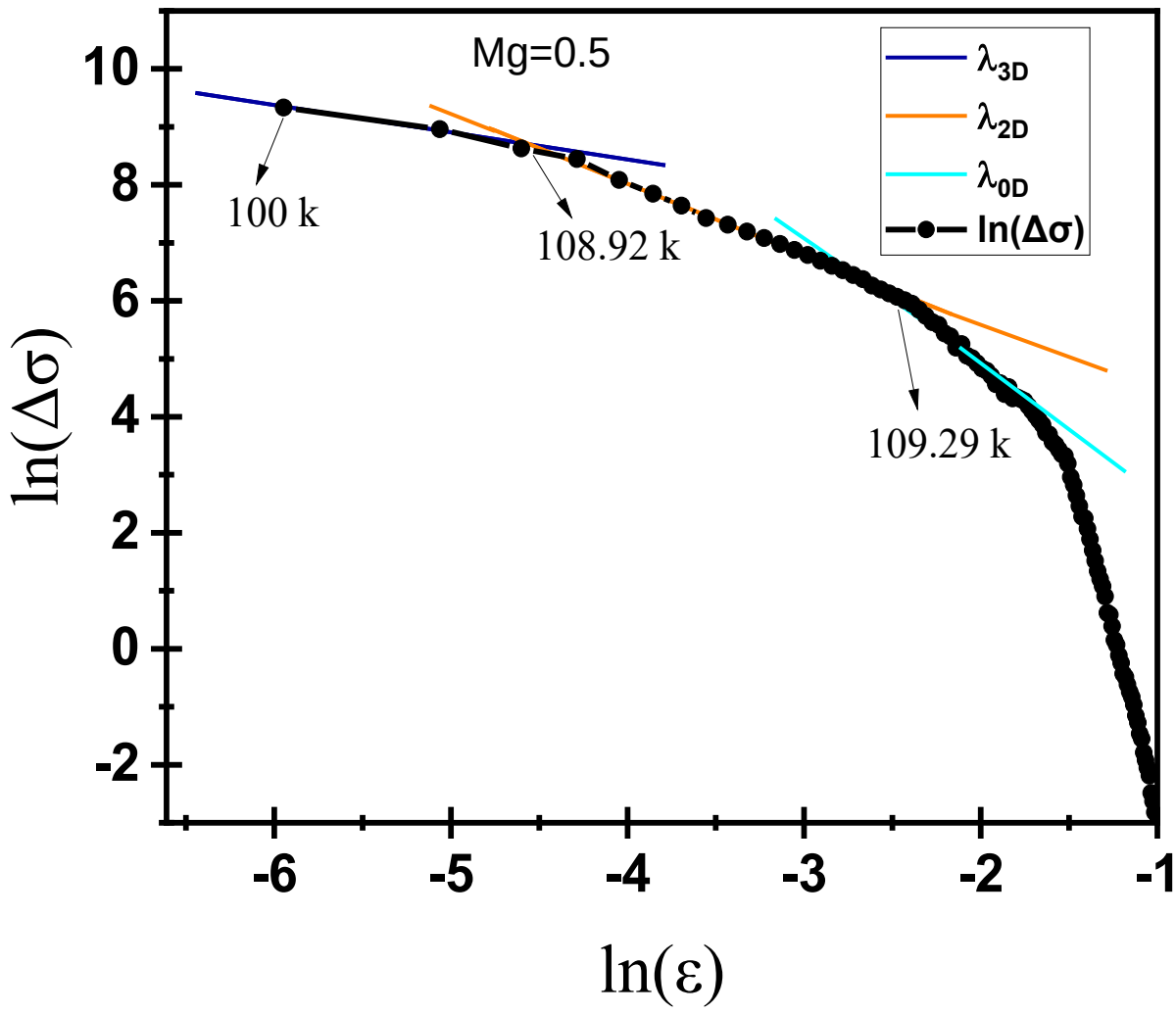

Fig 4.7c: ln($\Delta\sigma$) Vs ln(ε) depiction of a $(Cu_{0.5}Tl_{0.5})Ba_2(Ca_{1.5}Mg_{0.5})(Cu_{2.5}Cd_{0.5})O_{10-\delta}$

4.4 Conclusion:

In current dissertation infield magneto-conductivity and the excess conductivity analyses of $Cu_{0.5}Tl_{0.5}Ba_2(Ca_{2-y}Mg_y)(Cu_{2.5}Cd_{0.5})O_{10-\delta}(y = 0,0.25,0.5)$ samples is carried out. We have studied the impact of decreased inter-CuO_2 /CdO_2-plane distances on superconductivity of such samples. In the XRD analysis of such samples it is noticed that the volume of the unit cell increases and their c-axes lengths suppress with greater Mg doping. Increase in the unit cell's volume and reduction in c-axes lengths have shown enhancement of inter-plane couplings. It was expected that

superconducting properties of such samples will be enhanced because the density of carriers and inter-plane coupling is enhanced. However, superconducting properties are not enhanced in such samples. Compared to un-doped samples resistivity of Mg-doped samples increases whereas their zero resistivity critical temperature suppresses; un-doped samples have shown zero resistivity critical temperature at 102K whereas that Mg-doped samples is 96, 94K, respectively. The underlying route cause for this is the existence of mixed CuO_2/CdO_2 planes in such compounds; We have seen in our earlier research the enhancement of superconductivity in Mg doped $Cu_{0.5}Tl_{0.5}Ba_2\left(Ca_{2-y}Mg_y\right)(Cu_3)O_{10-\delta}y = (0,0.25,0.5)$ samples which contain only CuO_2 planes. Since such superconducting planes have Cd atoms that is heavier than the atoms of Cu and therefore it induce an-harmonic oscillations that induces pair breaking effects in the final compound. These studies have also shown that there is definitely involvement of phonons in the mechanism of high Tc superconductivity. With increased strength of applied external magnetic fields T_c(R=0) shifts towards lower temperatures values showing thermally activated flux flow across the pinning centers. Activation such thermally activated flow decreases with increased Mg-doping and enhance strength of applied field. The para-conductivity analyses of Mg-doped samples have displayed enhancement of coherence length along the c-axis, Fermi-velocity of carriers and critical current density. However, the thermodynamic decrease in Mg-doped samples that displayed vivid evidence of enhancement of microscopic Mg-doped samples' pinning centers.

Reference

[1] Khurram, A.A., Qurat-ul-Ain, Khan, N.A., Kameli, P.: Solid State Sci. 13, 2142 (2011)

[2] Tinkham, M.: Phys. Rev. Lett. 61, 1658 (1988)

[3] Woch, W.M., Zalecki, R., Kolodziejczyk, A., Sudra, H., Gritzner, G.: Supercond. Sci. Technol. 21, 085002 (2008)

[4] Sato, T., Nakane, H., Mori, N., Yoshizawa, S.: Physica C 357, 244 (2003)

[5] Ghosh, A.K., Bandyopadhyay, S.K., Barat, P., Sen, P., Basu, A.N.: Physica C 264, 255–260 (1996)

[6] Kaur, M., Srinibasan, R., Mehta, G.K., Kanjilal, D., Pinto, R., Ogale, S.B., Mohan, S., Ganesan, V.: Physica C 443, 61–68 (2006)

[7] Lawrence, W.E., Doniach, S. In Proceedings of the 12th International Conference on Low Temperature Physics, p. 361. Keigaku, Tokyo (1971)

[8] Abu Aly, A.I., Ibrahim, I.H., Awad, R.A., El-Harizy, A.: J. Supercond. Nov. Magn. 23, 1325 (2010)